

# Spectral evolution of hot hybrid white dwarfs I. Spectral analysis

Semih Filiz<sup>1</sup>, Klaus Werner<sup>1</sup>, Thomas Rauch<sup>1</sup>, and Nicole Reindl<sup>2</sup>

<sup>1</sup> Institut für Astronomie und Astrophysik, Kepler Center for Astro and Particle Physics, Eberhard Karls Universität, Sand 1, 72076 Tübingen, Germany

e-mail: filiz@astro.uni-tuebingen.de

<sup>2</sup> Landessternwarte Heidelberg, Zentrum für Astronomie, Ruprecht-Karls-Universität, Königstuhl 12, 69117 Heidelberg, Germany

Received 14 August, 2024; accepted 3 October, 2024

## ABSTRACT

*Context.* Hydrogen-rich white dwarfs (WDs) comprise the majority of the WD population, but are only rarely found at the very hot end of the WD cooling sequence. A small subgroup that exhibits both hydrogen and helium lines in their spectra, the so-called hybrid (or DAO) WDs, represents the majority of hydrogen-rich WDs at effective temperatures  $T_{\text{eff}} \approx 100$  kK.

*Aims.* We aim to understand the spectral evolution of hot hybrid WDs. Although small in number, they represent an evolutionary phase for most ( $\approx 75\%$ ) WDs.

*Methods.* We conducted a nonlocal thermodynamic equilibrium (NLTE) analysis with fully metal line blanketed model atmospheres for the ultraviolet (UV) and optical spectra of a sample of 19 DA and 13 DAO WDs with  $T_{\text{eff}} > 60$  kK. The UV spectra allow us to precisely measure the temperature through model fits to metal lines in different ionization stages. This enables us to place the WDs accurately on the cooling sequence.

*Results.* In contrast to earlier studies that typically relied on temperature measurements made from hydrogen lines alone, all DAOs in our sample are clearly hotter than the DAs. DAOs transform into DAs when they cool to  $T_{\text{eff}} \approx 75$ – $85$  kK, depending on their mass. Along the cooling sequence, we witness a gradual decrease in the abundance of helium and the CNO elements in the DAOs due to gravitational settling. Simultaneously, iron and nickel abundances increase up to the transition region because radiative forces act more efficiently on them. This is followed by a steady decline. We discuss the implications of our results on atomic diffusion theory and on the role of weak radiation-driven winds in hot hydrogen-rich WDs.

**Key words.** white dwarfs – spectral evolution – stars: evolution – stars: atmospheres – stars: abundances

## 1. Introduction

White dwarfs (WDs) represent the final stage in the evolution of low- and intermediate-mass stars ( $M < 8 M_{\odot}$ ). They are the predominant end products of stellar evolution. From the *Gaia* mission, approximately 359 000 high-confidence WD candidates were identified in the Milky Way (Gentile Fusillo et al. 2021b), and more than 37 000 WDs are spectroscopically confirmed (Kepler et al. 2021, and references therein). With the upcoming space-based gravitational-wave detector Laser Interferometer Space Antenna (LISA), optically faint WD binaries will be studied. This in turn will help us to uncover Galaxy regions that are otherwise hard to observe (Lamberts et al. 2019).

In addition to their substantial numbers, WDs present an incontrovertible prospect of investigating physics under extreme conditions. In this sense, hot WDs offer a unique opportunity besides connecting the final stages of stellar evolution to earlier phases. They are reliable sources for deriving atomic data of elements beyond the iron group (Rauch et al. 2012, 2014a,b, 2015a,b, 2016a,b, 2017a,b, 2020) and for testing theories of the influence of gravity on the fundamental constants (Hu et al. 2021).

In the aftermath of the asymptotic giant branch (AGB) phase, the post-AGB star enters the WD cooling sequence with either an H-rich (spectral type DA) or He-rich (spectral type DO) envelope of the main constituent. About three-quarters of all WDs

are born H-rich (Bédard et al. 2020), but along the cooling track, this fraction does not remain constant because atmospheric processes alter the main spectroscopic marker (Bédard et al. 2022). As in this case, the drastic change in the atmospheric composition is referred to as spectral evolution. In the course of cooling off, WD atmospheres are prone to transformation by multiple processes, such as mass loss, radiative levitation, gravitational settling, atomic diffusion, convection, and accretion. Our current understanding of the spectral evolution of WDs has been established through the collective efforts of nearly four decades, and addressing every milestone in this endeavor is beyond the scope of this introduction. Therefore, we only mention the required aspects and developments for hot H-rich and hybrid WDs (spectral type DAO) that show a weak He II  $\lambda 4686$  Å line. For an extensive review of the spectral evolution of WDs, we refer to Bédard (2024).

The presence of helium in the hot hydrogen-rich WD atmospheres has been the subject of several discussions. Extreme-ultraviolet (EUV) and X-ray observations of hot DA WDs revealed a flux deficiency in the shorter wavelengths (Vennes et al. 1988), which is opposed to what is expected for hot WDs with pure H envelopes. It was initially proposed that traces of He in the atmosphere provide the opacity for the observed EUV and X-ray flux deficiency. However, Vennes et al. (1988) demonstrated that the required amount of He could not be radiatively levitated. They showed that EUV observations can instead be

reproduced with models that consider stratified atmospheres in which a thin layer of H ( $M_{\text{H}}/M_* = 10^{-15}$ – $10^{-13}$ ) floats above the He envelope. However, this contradicts standard stellar evolution theory, which predicts  $M_{\text{H}}/M_* = 10^{-4}$  for the H envelope (Blöcker et al. 1997). Subsequent studies showed that the EUV and X-ray fluxes of several other hot DA WDs cannot be reproduced with stratified atmospheres (Vennes et al. 1989; Vennes 1992; Vennes & Fontaine 1992). Metal opacities were instead identified as the likely source of the observed flux deficiency in these objects.

The discovery of hybrid WDs (Koester et al. 1979) helped to clarify the situation. Bergeron et al. (1994) demonstrated that models with homogeneous atmospheres yielded better fits than stratified atmospheres in the optical spectra of DAO WDs (except for one object<sup>1</sup> at that time). Since the radiation pressure is proven insufficient to prevent the gravitational settling of He (Vennes et al. 1988), they suggested that weak mass-loss might induce the homogenized hybrid atmospheres. Bergeron et al. (1994) also reported that their analysis was heavily hindered by the Balmer-line problem (BLP), which commonly emerges in the optical spectra of hot DA and DAO WDs and prevents simultaneous fits to all Balmer lines with the same parameters. The authors concluded that the BLP is linked to the presence of metals in the atmosphere, which reinforced the idea that metal-driven winds shape the atmospheres of hot hybrid WDs. The BLP and the trace-metal connection was later supported by the quantitative and qualitative spectral analyses of Werner (1996) and Gianninas et al. (2010), respectively. On the other hand, the origin of the metals in hot WD atmospheres has been heavily debated because of the mismatch between observations and diffusion theory that assumes an equilibrium between gravitational settling and radiative levitation (Chayer et al. 1995a,b). Mass loss was mainly regarded as the missing ingredient in theoretical diffusion calculations. Only Barstow et al. (2014) and Preval et al. (2019) speculated that the accretion of planetary material might explain the observed metal abundances.

The occurrence of stellar winds in hot WDs cannot be shown directly because the expected mass-loss rates are too low (Unglaub & Bues 2000) for a spectroscopic detection in P Cygni profiles. Nonetheless, indications of mass loss can still be deduced from the spectra of hot WDs. The first indication for the occurrence of winds was the detection of ultra-highly excited (UHE) metals in the optical spectra of hot WDs (Werner et al. 1995). Because of the asymmetrical shapes of the line profiles, it was speculated that UHE features stem from shock fronts in the stellar wind. Reindl et al. (2019) showed that recurrent spectroscopic variations of UHE lines and the light curve can be explained with rotational modulation of a magnetosphere that traps the ejected material. In this case, magnetically confined wind shocks can heat the plasma to the required extreme temperatures ( $10^6$  K) for the occurrence of the UHE phenomenon. Another indirect evidence for radiation-driven winds was shown by Napiwotzki (1999). They reported a decreasing He abundance with decreasing luminosity in their hybrid WD sample.

Theoretical calculations of the influence of radiation-driven winds on the atmospheric composition by Unglaub & Bues (1998, 2000) revealed that mass-loss rates of  $\approx 10^{-11} M_{\odot}\text{yr}^{-1}$  can retard the gravitational settling of He in the hybrid atmospheres. The inevitable cessation of the mass loss expedites the effects of

<sup>1</sup> This object is an example for DAO WDs with stratified atmospheres, which are found at  $T_{\text{eff}} \leq 55$  kK (Manseau et al. 2016; Bédard et al. 2020) and advance through the DO-to-DA evolutionary channel (Manseau et al. 2016).

gravity, and a spectral transition from DAO to DA is expected. This paints a clear picture in the Kiel diagram, which has a well-defined theoretical wind limit. However, observations of hot DA and DAO WDs showed a lower effective temperature ( $T_{\text{eff}}$ ) range for the transition (Gianninas et al. 2010). Additionally, the measured temperature and surface gravity ( $\log g$ ) values of both H-rich and hybrid WDs revealed that DA and DAO WDs partially overlap along the cooling sequence (Bergeron et al. 1994; Napiwotzki 1999; Barstow et al. 2003b; Good et al. 2004; Gianninas et al. 2010, 2011). When we accept that the mass loss in hybrid WDs is strong enough to prevent He from sinking out of the atmosphere, then we have to ask why the winds of DAs with similar  $T_{\text{eff}}$  and  $\log g$  are insufficient to sustain He in the atmosphere. This indicates that other factor(s) in addition to  $T_{\text{eff}}$  and  $\log g$  are involved in inducing the spectral transformation along the cooling track. The scatter of hot DA and DAOs in the  $T_{\text{eff}}\text{-}\log g$  diagram was indeed speculated to be a consequence of the initial metallicity or of different masses (Unglaub & Bues 2000; Bédard et al. 2020). Therefore, our immediate aim is to measure the element abundances in UV spectra of hot DA and DAO WDs in order to determine the atmospheric and stellar parameters. We also wish to shed light on whether a well-defined limit exists in the Kiel diagram that separates DA and DAO WDs, and if the metal abundances change along the cooling track.

In this paper, we analyze the ultraviolet (UV) and optical spectra of DA and DAO WDs<sup>2</sup>. In Sect. 2, the sample selection and observations are described. We explain the spectral analysis procedure for measuring atmospheric and stellar parameters in Sects. 3 and 4. Finally, we discuss the implications of our results in Sect. 5 and give a brief summary in Sect. 6.

## 2. Sample selection and observations

We selected a sample of hot WDs with  $T_{\text{eff}} \geq 60$  kK, above which homogeneous hybrid WDs are found. Our sample comprised 13 DAO, and 19 DA WDs (Table B.1) for which the main selection criterion was the availability of archival Far Ultraviolet Spectroscopic Explorer (FUSE) or Space Telescope Imaging Spectrograph (STIS) spectra. All objects have archival FUSE spectra, except for WD 0939+262. Archival STIS spectra are present only for 4 DAOs and 8 DAs.

### 2.1. FUSE

We retrieved FUSE spectra for 31 objects observed with the low-resolution spectrograph (LWRS; resolving power  $R \approx 20\,000$ ) aperture from Mikulski Archive for Space Telescopes (MAST)<sup>3</sup>. The entire FUSE wavelength range (905–1188 Å) consists of eight overlapping segments. Therefore, an inspection of flux levels from each segment as well as each exposure was necessary. When any exposure-to-exposure flux variation exceeded  $\approx 10\%$ , we discarded the corresponding exposure. The majority of exposures made with the LiF1b channel suffer from a flux decrease because the detector area is shadowed by grid wires, known as the "worm" (FUSE Data Handbook<sup>4</sup>). When the overall flux

<sup>2</sup> Conventionally, the WD spectral classification is based on evaluated optical spectra. In this paper, we exclude secondary letters denoting weaker spectral features detected in other parts of the electromagnetic spectrum for simplicity (e.g., Z in the case of a metal detection for DAZ and DAOZ WDs).

<sup>3</sup> <https://archive.stsci.edu>

<sup>4</sup> <https://archive.stsci.edu/fuse/instrumenthandbook/contents.html>

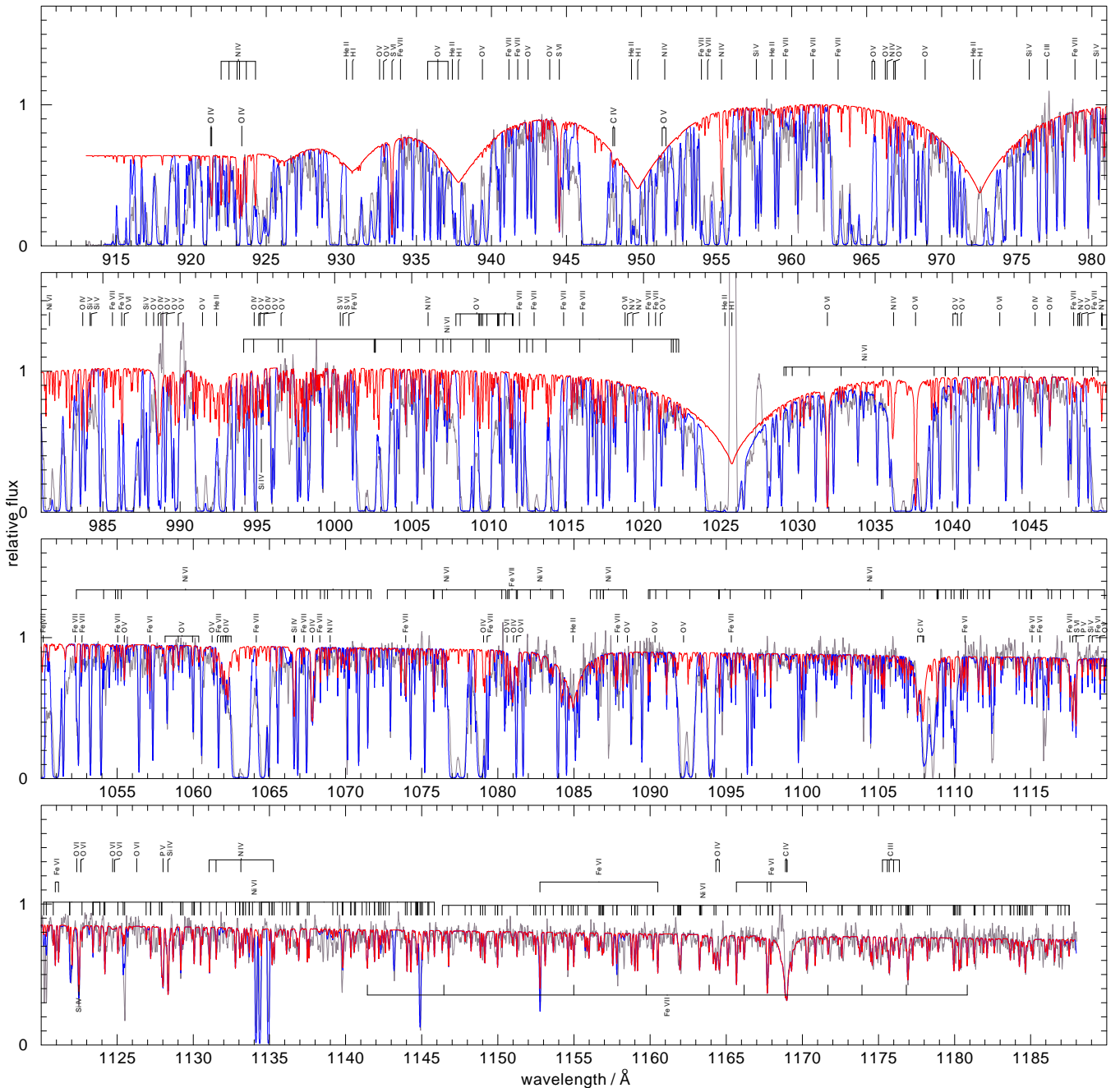


Fig. 1: FUSE spectrum (gray) of the DAO WD 2342+806 (red shows the model with  $T_{\text{eff}} = 83$  kK,  $\log g = 7.2$  ( $\text{cm/s}^2$ ), and blue shows the same model including the ISM lines). All model spectra displayed in this paper are convolved with Gaussians according to the instrument resolution. Additionally, all UV spectra are smoothed with a low-bandpass filter.

level of a particular LiF1b spectrum did not drastically deviate from the spectra of other channels, the wavelength range in which the worms prevailed was eliminated. Otherwise, the entire LiF1b spectrum was discarded, which was our action in most cases. Then, each available exposure from a particular segment was coadded into a single spectrum. Moreover, the coadded spectrum of each overlapping segment was then coaligned to already identified ISM lines and combined into a single composite spectrum. Finalized composite FUSE spectra of DAO WD 2342+806 and DA WD 2211-495 with their best-fit models are shown as examples in Figs. 1 and 2, respectively.

## 2.2. HST

The archival spectra of 12 sample objects were observed with the STIS on board the *Hubble* Space Telescope (HST) using the FUV-MAMA detector. For 9 of the objects (4 DAO and 5 DA), observations were carried out with the E140M grating ( $\approx 1144\text{--}1729$  Å,  $R \approx 45\,800$ ), and the remainder were observed with the E140H grating ( $R \approx 114\,000$ ), which consists of prime and secondary tilts. In the MAST archive, observations made with E140H only contain prime tilt with a central wavelength of 1416 Å, meaning that we only had access to the spectral range of 1317–1517 Å for these 3 DAs. When more than one observa-

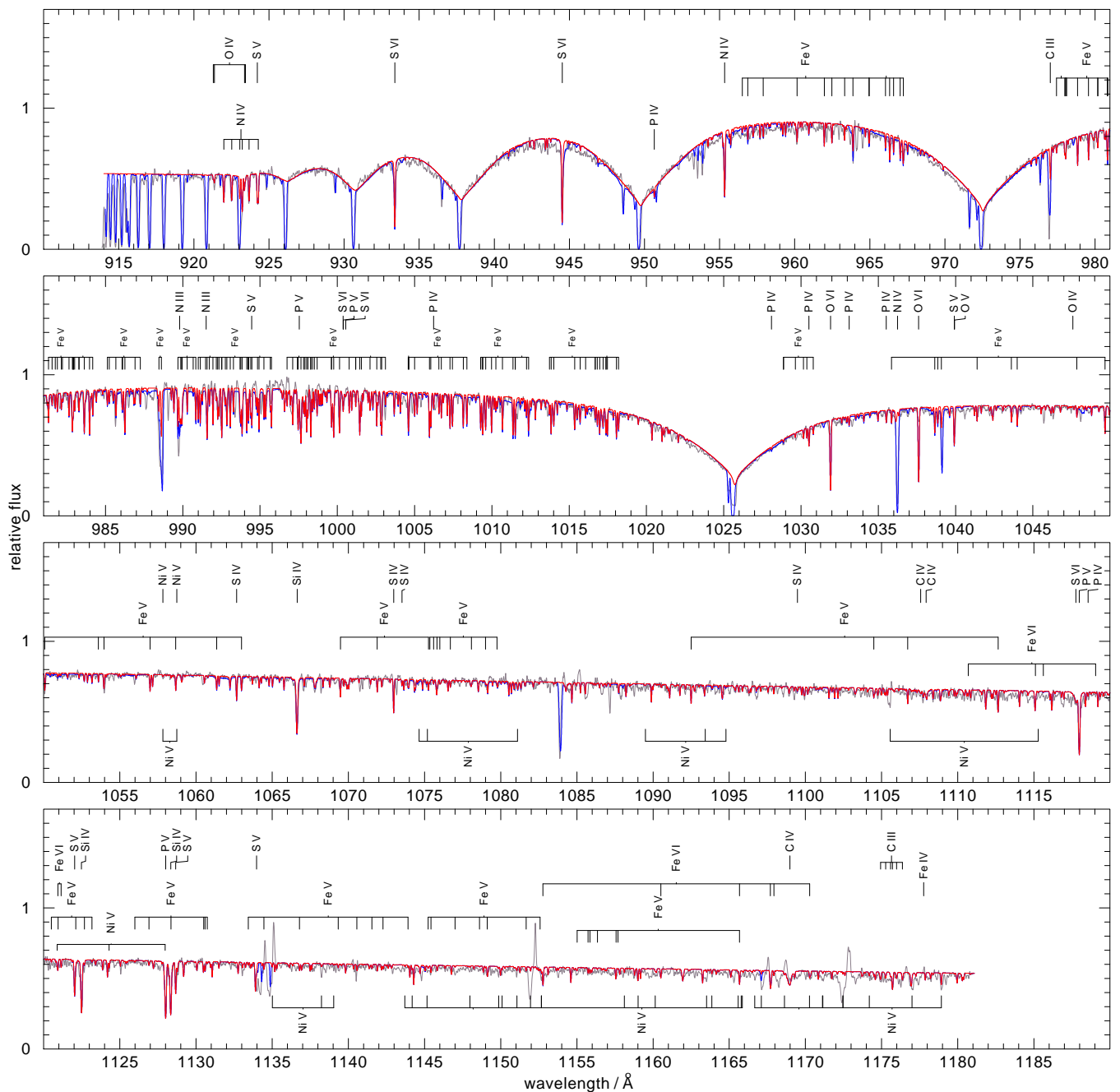


Fig. 2: FUSE spectrum of the DA WD 2211–495 (red shows the model with  $T_{\text{eff}} = 68$  kK,  $\log g = 7.4$ , and blue shows the model including the ISM lines).

tion was available, the observations were coadded to increase the signal-to-noise ratio (S/N). In Fig. A.1 and A.2, STIS spectra of WD 2342+806 (E140M) and WD 2211–495 (E140H), respectively, are shown as examples with their best-fit models.

### 2.3. Optical

Archival optical spectra for all sample objects were acquired from the Montreal White Dwarf Database (MWDD, [Dufour et al. 2017](#)), except for Longmore 1, WD 0851+090, WD 1111+552, and WD 2350–706. The typical resolution for the MWDD spectra is  $\approx 3\text{--}6$  Å. Observations of the MWDD spectra are described in detail by [Gianninas et al. \(2010,](#)

[2011\)](#), [Lépine et al. \(2011\)](#). We found no optical spectrum of WD 1111+552 and WD 2350–706, but archival Ultraviolet and Visual Echelle Spectrograph (UVES;  $R \approx 40\,000$ ) spectra are available for Longmore 1 and WD 0851+090. UVES spectra of WD 0621–376 and WD 2211–495 were also used to make comparisons. For the same reason, we acquired Sloan Digital Sky Survey (SDSS, [Abazajian et al. 2009](#)) spectra of three other DAs (WD 1056+516, WD 1342+443, WD 1827+778), which were also available in MWDD. We should note that for nine other objects (two DAOs and seven DAs) UVES and (four DAOs and five DAs), LAMOST spectra are available. However, conducting an extensive optical analysis is beyond the scope of this study. Therefore, we simply analyzed optical spectra to constrain  $\log g$

Table 1: Number of NLTE levels and lines of extended classical model ions.

	II	III	IV	V	VI
C	1, 0	56, 242	54, 295		
N	1, 0	34, 129	90, 547	54, 297	
O	1, 0	72, 322	83, 637	103, 729	54, 291
Si		17, 27	30, 102	25, 59	27, 74
P		3, 1	21, 25	18, 49	
S		1, 0	37, 150	39, 107	25, 48

**Notes.** Each cell in the table shows the number of NLTE levels and lines. The highest ionization stage of each element is only included as ground state and is not listed here.

and investigated whether common ground between optical and UV results can be found.

#### 2.4. Interstellar absorption and reddening

Absorption lines from the interstellar medium (ISM) may heavily contaminate FUSE spectra, and they need to be disentangled from photospheric lines to precisely determine the atmospheric parameters. Therefore, we identified ISM lines employing the line-fitting procedure OWENS (Lemoine et al. 2002; Hébrard et al. 2002; Hébrard & Moos 2003), which individually models radial and turbulent velocities, column densities, temperatures, and chemical compositions of different clouds. In general, the detected ISM lines included D I, H I, H<sub>2</sub>, C I-III, N I-III, O I, P II, S II-III, Ar I, and Fe II.

We determined the interstellar reddening for each star by comparing the model fluxes to Tycho2, SDSS, and 2MASS magnitudes. The model spectra were normalized to fluxes observed with the filter in the longest wavelength when no 2MASS K flux was available. Then, the reddening law by Fitzpatrick (1999) with  $R_V = 3.1$  was employed to determine the  $E(B-V)$  values of the sample objects.

### 3. Spectral analysis

We conducted a spectral analysis with the Tübingen Model-Atmosphere package (TMAP<sup>5</sup>, Werner & Dreizler 1999; Werner et al. 2003, 2012), which computes nonlocal thermodynamic equilibrium (NLTE) model atmospheres in radiative and hydrostatic equilibrium assuming plane-parallel geometry. The opacities of H, He, C, N, O, Si, P, S, Fe, and Ni were included in our models. Classical model atoms (hydrogen to sulfur) were constructed with atomic data from the Tübingen Model Atom Database (TMAD, Rauch & Deetjen 2003). For Fe and Ni, we used the Tübingen Iron-group opacity interface (TIRO, Rauch & Deetjen 2003; Müller-Ringat 2013), which uses a statistical approach to manage the vast number of atomic levels and line transitions by combining energy levels and sampled lines of a particular ion to super levels and super lines, respectively. Additionally, we employed the Stark broadening tables of Tremblay & Bergeron (2009) and Schoening & Butler (1989) to calculate the synthetic line profiles of H I and He II.

Metal line blanketed models were initially built with relatively small model atoms for elements up to sulfur to avoid numerical instabilities and to optimize computation time. Subse-

Table 2: Number of super levels and super lines of the iron and nickel model atoms.

	Super Levels	Super Lines	Sample Lines
Fe IV	7	25	3102371
Fe V	7	25	3266247
Fe VI	7	25	991935
Fe VII	7	24	200455
Fe VIII	7	27	19587
Fe IX	1	0	0
Ni IV	7	25	2512561
Ni V	7	27	2766664
Ni VI	7	27	7407763
Ni VII	7	25	4195381
Ni VIII	7	27	1473122
Ni IX	1	0	0

quently, line formation iterations were executed with extended model atoms by keeping the atmospheric structure fixed. An overview of the extended classical model atoms is listed in Table 1. Additionally, ionization stages IV - IX were included for Fe and Ni (Table 2). We customized model atoms for each object by adjusting the ionization stages of a particular element according to individual parameter ranges.

The wide range in temperature and surface gravity and the numerous parameters of our sample did not facilitate either creating an extensive model atmosphere grid or taking a statistical approach in the spectral analysis. Instead, our method involved an iterative process of line-profile fitting by consecutively computing a series of models while improving the parameters and decreasing the uncertainty. Our analysis procedure is summarized below.

1. Calculate a small grid of pure H and H+He models close to the literature  $T_{\text{eff}}$  and  $\log g$  values of DA and DAOs, respectively.
2. Roughly constrain  $T_{\text{eff}}$ ,  $\log g$ , and He abundance from the UV H and He lines.
3. Compute a series of fully metal-line blanketed models around the updated values.
4. Refine  $T_{\text{eff}}$  and determine the metal abundances by fitting the UV metal lines.
5. Improve  $\log g$  and He abundance from the optical spectra.
6. Recalculate models with the fine-tuned parameters.

#### 3.1. DAO analyses

##### 3.1.1. Effective temperature and surface gravity

H+He models for each object were computed assuming a solar He content, with  $T_{\text{eff}}$  and  $\log g$  close to the values determined by Gianninas et al. (2010) through their analysis of optical spectra via Balmer-line fitting. When the latter authors did not analyze a particular object, we selected values close to those derived by Ziegler (2012). Then, we constrained  $T_{\text{eff}}$  and  $\log g$  from the Lyman lines in the FUSE spectra. In the next step, we included metal opacities in our model atoms. A set of strategic lines from several ions was identified since the absence or presence of a particular line would indicate a certain  $T_{\text{eff}}$ . While keeping  $\log g$  fixed, we exploited multiple ionization equilibria such as C III/C IV, N IV/N V, O IV/O V/O VI, Fe V/Fe VI/Fe VII/Fe VIII,

<sup>5</sup> <http://astro.uni-tuebingen.de/~TMAP>

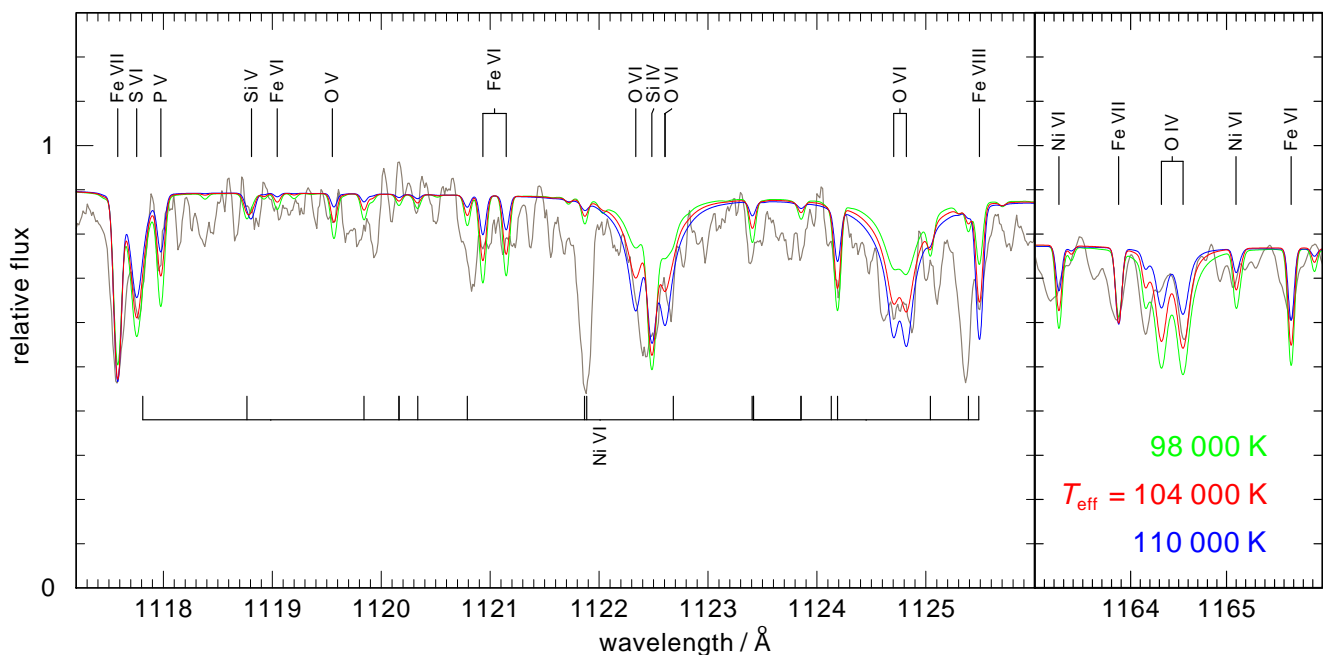


Fig. 3: Details of the FUSE spectrum of the DAO WD 0500–156 compared to three models with different temperatures  $T_{\text{eff}} = 104 \pm 6$  kK,  $\log g = 7.2$ .

and Ni v/Ni vi to constrain  $T_{\text{eff}}$  (Fig. 3). A detailed overview of each element is presented in Sect. 3.1.3.

Contamination due to interstellar H I and other interstellar absorption hinders the correct assessment of the local continuum in the far-UV range. This in turn affects the precise measurement of  $\log g$  via fitting the Lyman lines. Thus, investigation of optical spectra was necessary to verify our  $\log g$  values. In general, the parameters determined with UV analysis lay within the error range of the Balmer-line analysis.

### 3.1.2. He abundance

A preliminary He abundance was determined from isolated lines of He II  $n = 2 \rightarrow n'$  line series in the FUSE range. While we finetuned the temperature and gravity, the He abundance was further adjusted accordingly. Finally, we compared and, if necessary, modified our previous measurement by using He II  $\lambda 1640 \text{ \AA}$  ( $n - n' = 2 - 3$ ) and He II  $\lambda 4686 \text{ \AA}$ , which are the optimal lines to adjust the He abundance in their respective wavelength regions.

### 3.1.3. Metal abundances

**Carbon.** The C IV  $\lambda\lambda 1107, 1169 \text{ \AA}$  doublet was mainly used to determine the C abundance. In several cases, C IV  $\lambda 1169 \text{ \AA}$  is contaminated by an airglow line. When this was the case, we only relied on C IV  $\lambda 1107 \text{ \AA}$ . Although weak C III features can be observed below 100 kK, only WD 2342+806 displays the C III  $\lambda 1175 \text{ \AA}$  multiplet, which is a blend with N VI lines. The STIS wavelength range contains C IV multiplets at 1198 and 1239  $\text{\AA}$  as well as the C IV resonance doublet. Without exception, the line fits of the former two agree with the other C lines from the FUSE spectra, whereas the latter is weaker in our models. However, a quick inspection revealed that this must be due to ISM contribution. We achieved a good fit to the line cores of

the photospheric components, which are clearly separated from the blueshifted ISM component.

**Nitrogen.** The relative strengths of identified N IV and N V lines in the FUSE range can be exploited to confine  $T_{\text{eff}}$  within a rather wide range. The N IV  $\lambda 923 \text{ \AA}$  multiplet and the N IV  $\lambda 955 \text{ \AA}$  singlet disappear around 120 kK, whereas N V  $\lambda 1048.2 \text{ \AA}$  and N V  $\lambda 1049.7 \text{ \AA}$  quickly become weaker below 90 kK. The latter two are blended with ISM lines and cannot be identified in our sample. Therefore, the N IV  $\lambda 923 \text{ \AA}$  multiplet and the N IV  $\lambda 955 \text{ \AA}$  singlet were mainly used to determine the N abundance. When STIS spectra were available, the N V  $\lambda\lambda 1238.2, 1242.8 \text{ \AA}$  resonance doublet and the N IV  $\lambda 1718.5 \text{ \AA}$  were used as well. Compared to our photospheric models, we encountered a stronger N V resonance doublet in the observations of WD 1957+225 and WD 2226–210, which is expected to be dominated by interstellar absorption.

**Oxygen.** Multiple O IV, O V, and O VI lines are detectable in the FUSE spectra. A rather tight constraint can be made with the O ionization balance since O lines strongly react to  $T_{\text{eff}}$  changes. A weak O VI doublet at 1124  $\text{\AA}$  becomes visible around 95 kK and becomes stronger with increasing  $T_{\text{eff}}$ , in contrast to the O IV lines (Fig. 3). At 110 kK, the O V lines in the FUSE wavelength range still display strong features (Fig. 4). However, above this temperature and below 90 kK, they diminish quickly. We encountered problems with the O VI  $\lambda\lambda 1031.9, 1037.6 \text{ \AA}$  resonance doublet of the objects with  $T_{\text{eff}}$  below 115 kK. Without exception, the line cores are too deep in our final models. This issue was also reported by Rauch et al. (2007) and Werner et al. (2018b). In the STIS wavelength range, O V  $\lambda 1371.7 \text{ \AA}$  and O IV  $\lambda\lambda 1338.6, 1342.9, 1343.5 \text{ \AA}$  were identified. STIS spectra of WD 1957+225 and WD 2226–210 display O VI  $\lambda 1291 \text{ \AA}$ . However, in both cases, the observations show very broad features, and we were unable to model this line well.

**Silicon.** The most prominent silicon lines are Si IV  $\lambda\lambda 1066.61, 1066.65 \text{ \AA}$  and Si IV  $\lambda\lambda 1122, 1128 \text{ \AA}$  in

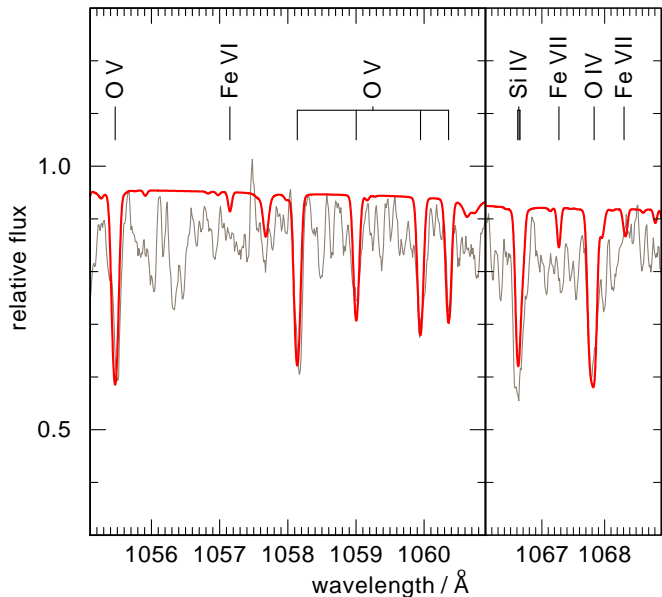


Fig. 4: Sections of the FUSE spectrum (gray) of the DAO WD 1111+552 showing the ionization balance of O IV and O V (red shows the model with  $T_{\text{eff}} = 111$  kK,  $\log g = 7.1$ ).

the FUSE range. However, Si IV  $\lambda$  1066 Å is blended with interstellar absorption. Therefore, the Si IV  $\lambda\lambda$  1122, 1128 Å doublet was used to determine the Si abundance. Only three objects with  $T_{\text{eff}}$  above 110 kK display a weak Si V  $\lambda$  1118.8 Å feature. Additionally, STIS spectra show the Si IV  $\lambda\lambda$  1394, 1402 Å resonance doublet, which is dominated by interstellar absorption, like the other two resonance lines (C IV, N V) identified in the STIS spectra. As opposed to the FUSE spectra, we detected Si V lines (Si V  $\lambda\lambda$  1245.7, 1251.4, 1276 Å) above 97 kK, which become stronger with increasing  $T_{\text{eff}}$ .

**Phosphorus.** The P abundances were determined by fitting the P V  $\lambda\lambda$  1118, 1128 Å resonance doublet. The other detected P V lines are quite weak and blend with other lines. Our DAOs are too hot to show P IV lines. No phosphorus lines were detected in the STIS spectra.

**Sulfur.** We identified the S VI  $\lambda\lambda$  933, 945 Å resonance doublet, S VI  $\lambda$  1000 Å, and S VI  $\lambda$  1117.7 Å in the FUSE spectra. Only one object resides in the temperature range in which S V lines can be displayed. Only S VI  $\lambda$  1419.4, 1419.7 Å and S VI  $\lambda$  1423.8 Å were detected in the STIS spectra of WD 0439+466 and WD 2342+806.

**Iron.** Prominent Fe VI - VIII lines were detected in the FUSE spectra, and they serve as excellent  $T_{\text{eff}}$  indicators. In Fig. 3, the  $T_{\text{eff}}$  assessment of WD 0500-156 is depicted as an example. As opposed to Fe VI, the relative strength of the Fe VIII lines intensifies above 98 kK, whereas the increase is minor for the Fe VII lines. At 110 kK, the Fe VIII lines become too strong, while the Fe VI lines weaken substantially. In addition to the mentioned ions, Fe V lines were also identified in the STIS spectra of objects below 100 kK (Fig. 5).

**Nickel.** FUSE spectra contain many Ni VI lines. The line strength of Ni VI lines diminishes quickly above 100 kK (Fig. 3). In the STIS spectra of WD 0439+466 and WD 2342+806, a number Ni V and Ni VI lines were identified (Fig. 6).

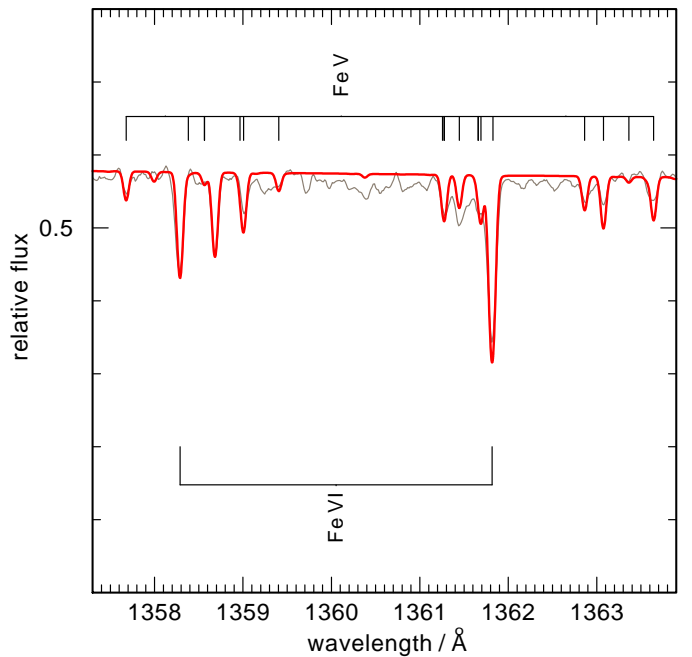


Fig. 5: Section of the STIS spectrum (gray) of the DAO WD 0439+466 (red shows the model with  $T_{\text{eff}} = 97$  kK,  $\log g = 7.0$ ).

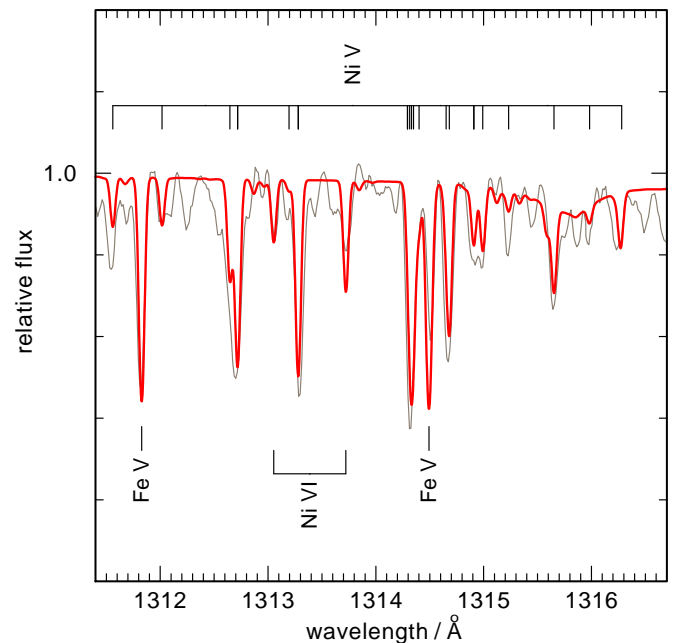


Fig. 6: Detail of the STIS spectrum (gray) of the DAO WD 2342+806 (red shows the model with  $T_{\text{eff}} = 83$  kK,  $\log g = 7.2$ ).

## 3.2. DA analyses

### 3.2.1. Effective temperature and surface gravity

We followed the same procedure as for the DAOs, but started by computing pure H models with literature values of  $T_{\text{eff}}$  and  $\log g$  (Gianninas et al. 2010, 2011; Barstow et al. 2014). In addition to adding the metal opacities, we also included a small amount of He in our model atmospheres. In their far-UV analy-

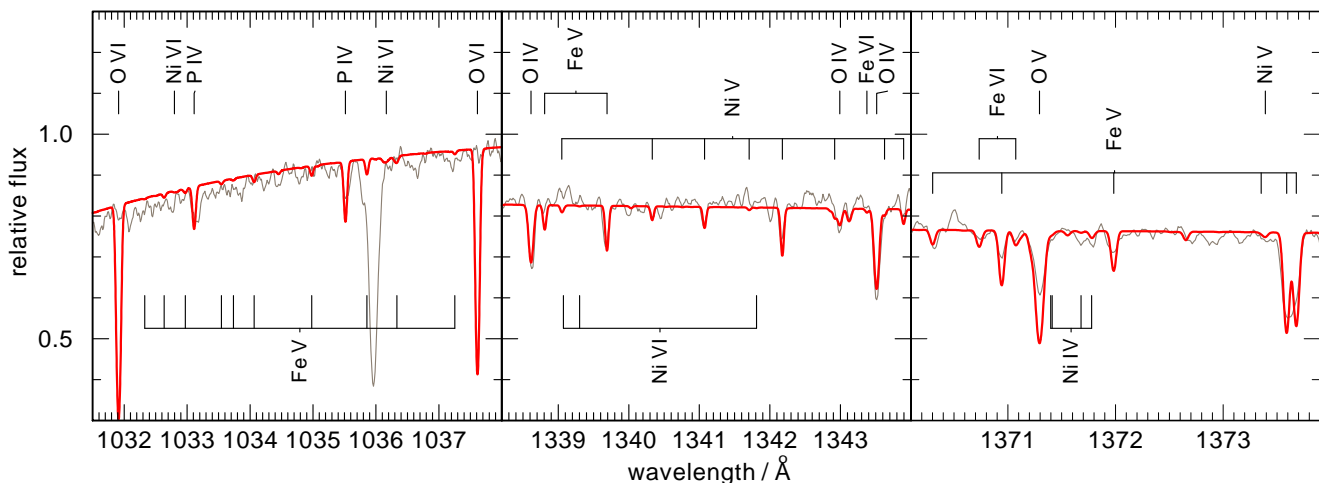


Fig. 7: Sections of FUSE (left panel) and STIS (middle and right panels) spectra (gray) of the DA WD 0232+035 (red shows the model with  $T_{\text{eff}} = 63$  kK,  $\log g = 7.5$ ), illustrating stratification effects on oxygen ions.

sis of G191-B2B, Rauch et al. (2013) opted for  $\log \text{He} < -4.7$  (mass fraction) as an upper limit. Since G191-B2B resides at the lower limit of the temperature criterion in our sample selection, this value was chosen as our starting He abundance and was adjusted to upper limits from He II  $n - n' = 2 - 11$  line series for each object. Additionally, we were able to fine-tune the upper limit with He II  $\lambda 1640$  Å for the objects with STIS spectra. Since the DAs in our sample have considerably lower temperatures than the DAOs, the ionization equilibria that we relied on also slightly altered (C III/C IV, N III/N IV/N V, O IV/O V/O VI, P IV/P V, S IV/S V/S VI, Fe V/Fe VI/Fe VII, and Ni V/Ni VI). Because of the low metal abundance and poor data quality, it was not possible to use the ionization balance of multiple elements in some cases. For these objects, higher error limits were imposed. In contrast to the DAO WDs,  $\log g$  values determined utilizing Lyman lines were not compatible with the Balmer lines. Therefore, we readjusted  $\log g$  according to the Balmer lines. However, in some cases, the disparity between the Lyman and the lower-order Balmer lines (e.g.,  $H\alpha$  and  $H\beta$ ) was too large, but the surface gravity determined from Lyman lines completely agreed with the higher-order Balmer lines. Since fitting higher-order Balmer lines corresponds to a more accurate  $\log g$  measurement (Werner 1996) and  $T_{\text{eff}}$  could be tightly constrained from UV, we opted in these cases for  $\log g$  measured in the UV and adopted a larger error margin.

### 3.2.2. Metal abundances

**Carbon.** The C III  $\lambda 1175$  Å multiplet was mainly used to determine C abundances. Multiple objects show a weak C IV  $\lambda 1169$  Å doublet. Similar to DAOs, this feature is contaminated in several FUSE spectra. When HST spectra were available in addition to C IV multiplets at 1198 and 1239 Å, we used the C IV  $\lambda\lambda 1548, 1550$  Å resonance doublet to confirm the C abundance.

**Nitrogen.** Most of the sample objects display the N IV multiplet at 923 Å and the singlet at 955 Å. N III  $\lambda 991$  Å was also identified in the spectra of objects with  $T_{\text{eff}} \leq 75$  kK. However, this line is blended with a Fe V line, and it would be unrealistic to determine the N abundance with it, although it is still useful for assessing the temperature with the N III/N IV ionization balance.

Therefore, the former two lines were mainly used to determine the N abundance. When the STIS spectrum was present, we exploited the N V  $\lambda\lambda 1238.2, 1242.8$  Å resonance doublet as well.

**Oxygen.** In the FUSE spectra of multiple objects, a weak O VI  $\lambda\lambda 1031.9, 1037.6$  Å resonance doublet was identified. A handful of objects display the short-wavelength component of the O IV 921–923 Å multiple, but the other component is a blend with the N IV  $\lambda 923$  Å multiplet. No additional oxygen lines were identified in the FUSE spectra. We detected O V  $\lambda 1371.7$  Å and O IV  $\lambda\lambda 1338.6, 1342.9, 1343.5$  Å in the STIS spectra. However, it was not possible to achieve a simultaneous fit to the lines of all three ionization stages (see Fig. 7). We further discuss this in Sect. 5.

**Silicon.** The Si IV  $\lambda\lambda 1066.61, 1066.65$  Å, and Si IV  $\lambda\lambda 1122, 1128$  Å doublets were mainly used to determine the Si abundance, which agreed with fits to the Si IV resonance lines. The Si III lines were identified.

**Phosphorus.** The P V  $\lambda\lambda 1118, 1128$  Å resonance doublet was identified. Objects below  $\approx 70$  kK also display P IV  $\lambda\lambda 950, 1028$  Å. No other P lines were identified in the STIS spectra.

**Sulfur.** Multiple cooler objects show the S IV  $\lambda\lambda 1072.97, 1073.52$  Å doublet. This line quickly weakens above 70 kK. In addition to S V  $\lambda 1028$  Å, S V  $\lambda 1222$  Å, and S V  $\lambda 1501.7$  Å, the S VI resonance doublet was also identified. However, in multiple cases, we encountered a similar problem with the O VI resonance doublet, in which the line cores were slightly stronger in our models.

**Iron and nickel.** Numerous Fe V and Fe VI as well as Ni V and Ni VI lines can be detected in FUSE and STIS spectra. The line strengths of both Fe VI and Ni VI start to diminish around 80 kK, whereas Ni V and Fe V become stronger.

## 4. Masses

We relied on the atmospheric parameters from our spectroscopic analysis to disclose the masses of the sample objects. To interpolate masses from the Kiel ( $T_{\text{eff}}-g$ ) diagram, we followed the



same steps as Reindl et al. (2023) and used the `griddata`<sup>6</sup> function in Python, which can rescale data points to the unit grid before making the interpolation. To estimate the Kiel masses, we considered the evolutionary tracks by Renedo et al. (2010) and Hall et al. (2013) (Fig. 8), which were devised for CO-core WDs (metallicity  $Z = 0.01$ ) and He-core WDs, respectively. However, none of the object spectroscopic parameters match the He-core tracks. The uncertainties were assessed using a Monte Carlo method. We found that DAOs in our sample ( $\langle M_{\text{DAO}} \rangle = 0.55 M_{\odot}$ ,  $\sigma = 0.02 M_{\odot}$ ) are on average less massive than DAs ( $\langle M_{\text{DA}} \rangle = 0.59 M_{\odot}$ ,  $\sigma = 0.05 M_{\odot}$ ), which was also found by Gianninas et al. (2010), Bédard et al. (2020), and Reindl et al. (2023).

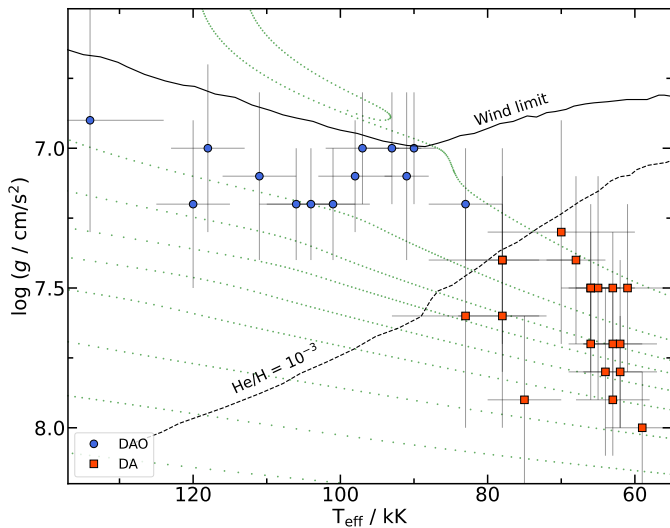


Fig. 8: Sample objects illustrated in the Kiel diagram. The dotted lines are evolutionary tracks of H-rich WDs ( $Z = 0.01$ ) from Renedo et al. (2010), representing in order 0.525, 0.570, 0.593, 0.609, 0.632, 0.659, 0.705, 0.767, and 0.837  $M_{\odot}$ . The solid and dashed black lines correspond to the theoretical wind limit and to the He abundance ( $N(\text{He})/N(\text{H}) = 10^{-3}$ ) calculated with the predicted mass-loss rates by Unglaub & Bues (2000, see their Fig. 6), respectively. The latter also coincides with the approximate optical detection limit of He.

## 5. Results and discussion

In this section, we present the general outcome of the spectral analysis and discuss the implications of the results.  $T_{\text{eff}}$ ,  $\log g$ , and the mass fractions of the elements are listed in Table B.2. The abundance of a particular element for all objects is also depicted in the Kiel diagram in comparison to the solar values (Fig. 9 and 10). Moreover, in Fig. 11, a comparison between metal abundances of DA WDs and theoretical diffusion calculations by Chayer et al. (1995b) and Vennes et al. (1996) is shown.

### 5.1. Mass loss and accretion

The winds of hot stars mainly emerge due to radiative forces acting on the metals. The metals in turn transfer momentum with Coulomb collisions to H and He, on which the radiative forces are very low (Krtićka et al. 2020). Unglaub & Bues (1998, 2000)

showed that chemically homogeneous winds could prevent gravitational settling of He in DAO atmospheres. When the WD crosses the wind limit and mass-loss ceases, He can no longer be sustained in the atmosphere, and a quick transition from DAO to DA is then expected.

This is exactly what we observe. The DAO WDs in our sample exhibit a solar He content at high  $T_{\text{eff}}$ . As the temperature decreases, the He abundance diminishes as well (Fig. 10). While CNO abundances follow the same trend (Fig. 9), other light metals are slightly subsolar. He is more rapidly depleted than CNO, as predicted by Unglaub & Bues (2000). In contrast, the Fe and Ni abundances of DAOs exceed the solar value (Fig. 10), excluding Longmore 1, WD 1111+552, and WD 1957+225, which are comparable to the Sun. Interestingly, the latter three also display solar He abundance. This implies that the effects of a weak stellar wind are prominent, while gravitational settling did not influence the photospheric abundances (Werner et al. 2018b). An increase in the abundances of heavy elements already indicates the influence of the radiative levitation (Rauch et al. 2016a), which can be noted in the case of WD 2226–210 because it, in contrast, has a lower He abundance than other objects with similar  $T_{\text{eff}}$ . Therefore, we argue that the abundance pattern of the remaining objects signifies an interplay between diffusion and stellar winds (Werner et al. 2018a; Löbbling et al. 2020).

In contrast to DAOs, CNO is extremely depleted in DA atmospheres, whereas the decrease in other light metals is less severe, especially for P. On the other hand, both Fe and Ni abundances are roughly solar. However, a trend is apparent here: With decreasing  $T_{\text{eff}}$  and increasing  $\log g$ , the Fe and Ni abundances diminish (Fig. 10). This implies that atomic diffusion is the main driving mechanism in the DA atmospheres (Werner et al. 2019). However, as we showed in Fig. 11, the comparison of the observed abundance pattern of DA WDs to theoretical diffusion calculations of Chayer et al. (1995b) and Vennes et al. (1996) revealed inconsistencies, except for iron. Different results between observations and the diffusion theory were also previously reported in several studies (Chayer et al. 1995a,b; Barstow et al. 2003b; Dobbie et al. 2005; Good et al. 2005a; Werner et al. 2007; Rauch et al. 2013; Barstow et al. 2014; Preval et al. 2019). The common ground in these papers was that at least one more mechanism is required to explain the discrepancy and should be included in theoretical calculations in addition to equilibrium theory. Competing ideas were that either weak mass-loss or accretion shapes the observed abundance pattern.

The mismatch in the Si abundance is particularly curious because Si is the only element that was consistently found in all previous studies to be more abundant than predicted by diffusion theory. Barstow et al. (2014) stated that overabundant phosphorus and silicon resemble the bulk material of terrestrial planets. The authors argued that the observed metal abundances arise due to accretion from short-lived gaseous disks rather than innately containing them. Then, accreted elements are radiatively levitated in the atmosphere, hence possibly marking the source of accretion as tidally disrupted planetary debris. Preval et al. (2019) showed that hot DA WDs in their sample exhibited Fe and Si abundances that were higher by an order of magnitude than the theoretical estimates. The authors interpreted the overabundance of metals as an indication of ongoing accretion from external sources. The existence of gaseous and dusty debris disks around WDs is indeed very well established (Jura 2003; Manser et al. 2016, 2020), and there is strong evidence that the debris disks originate in tidally disrupted planetary material (Gänsicke et al. 2019; Manser et al. 2019; Cunningham et al. 2022). However, to the best of our knowledge, the  $T_{\text{eff}}$  of any observed WD hosting a

<sup>6</sup> <https://docs.scipy.org/doc/scipy/reference/generated/scipy.interpolate.griddata.html>

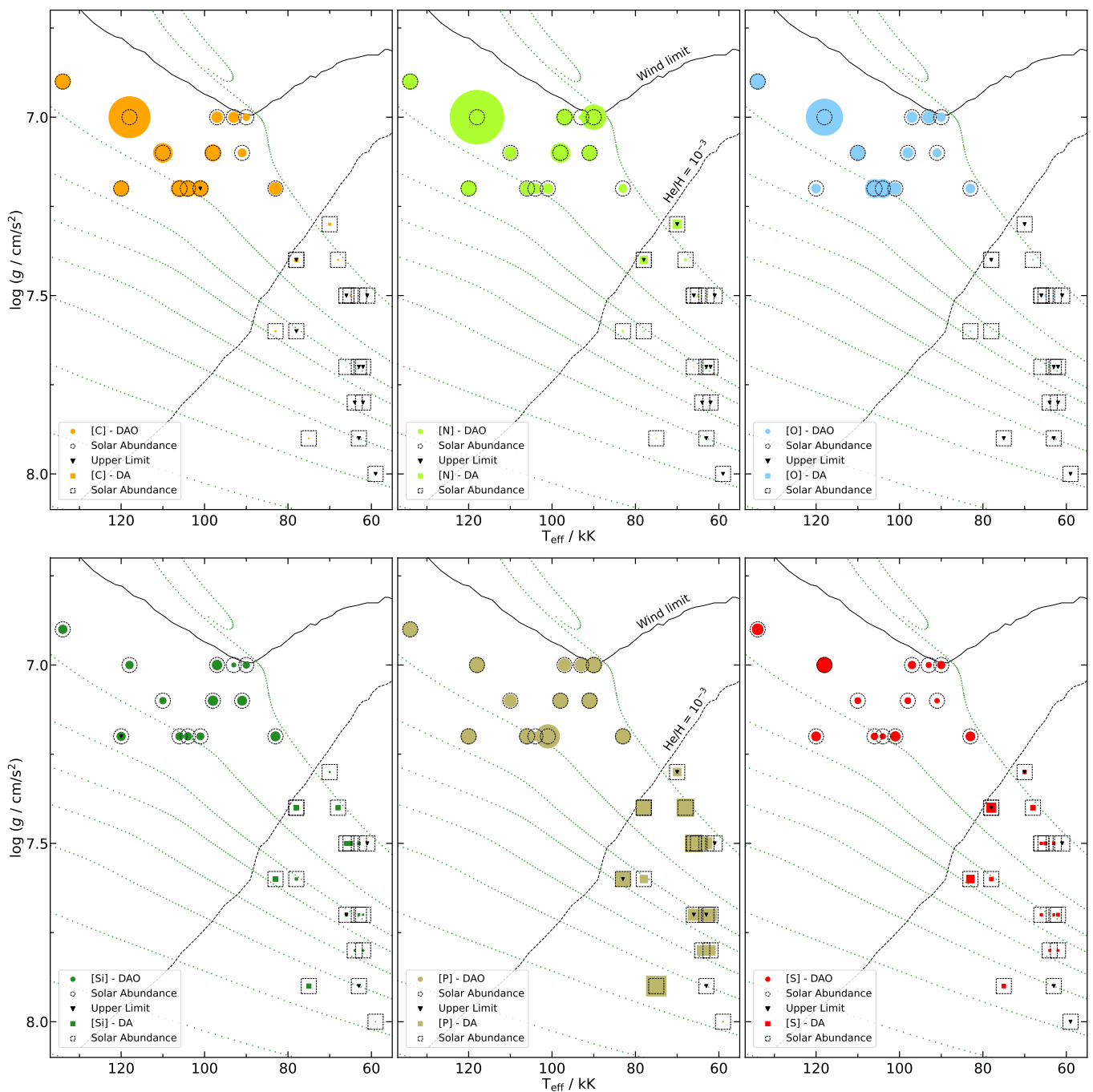


Fig. 9: Element abundances of our sample objects in the Kiel diagram (panels from upper left to lower right: C, N, O, Si, P, and S). The abundances are illustrated with filled circles and squares for DAOs and DAs, respectively. The symbol size is proportional to the mass fraction of the respective element. The dashed symbols represent solar values (Asplund et al. 2009). The upper limits are marked with an upside triangle, which does not scale with the abundances

debris disk does not exceed  $\sim 30$  kK (Koester et al. 2014; Manser et al. 2020; Melis et al. 2020; Gentile Fusillo et al. 2021a).

From the theoretical standpoint, Chayer et al. (1997) demonstrated that when either accretion or mass loss is included in the diffusion calculations, the observed overabundance of Si for a WD with  $T_{\text{eff}} = 60$  kK and  $\log g = 7.36$  can be explained. Moreover, Wesemael et al. (1984) explored the possibility of accretion from the M dwarf companion to Feige 24 as the source of the observed element abundances. Assuming a mass-loss rate of  $10^{-13}$

$M_{\odot}\text{yr}^{-1}$  for the M dwarf, they calculated the ram pressure in the stellar wind midway and compared this to the radiative pressure gradient of the WD. Accordingly, they demonstrated that the intense radiation field of the WD ( $T_{\text{eff}} \approx 60$  kK) can substantially retard the accretion rate and counteract the accretion. Since our sample objects have similar or higher  $T_{\text{eff}}$ , first, any grain material originating from supposed planetary debris would be sublimated due to the high luminosity of our objects compared to their cooler counterparts (von Hippel et al. 2007). Second, it is

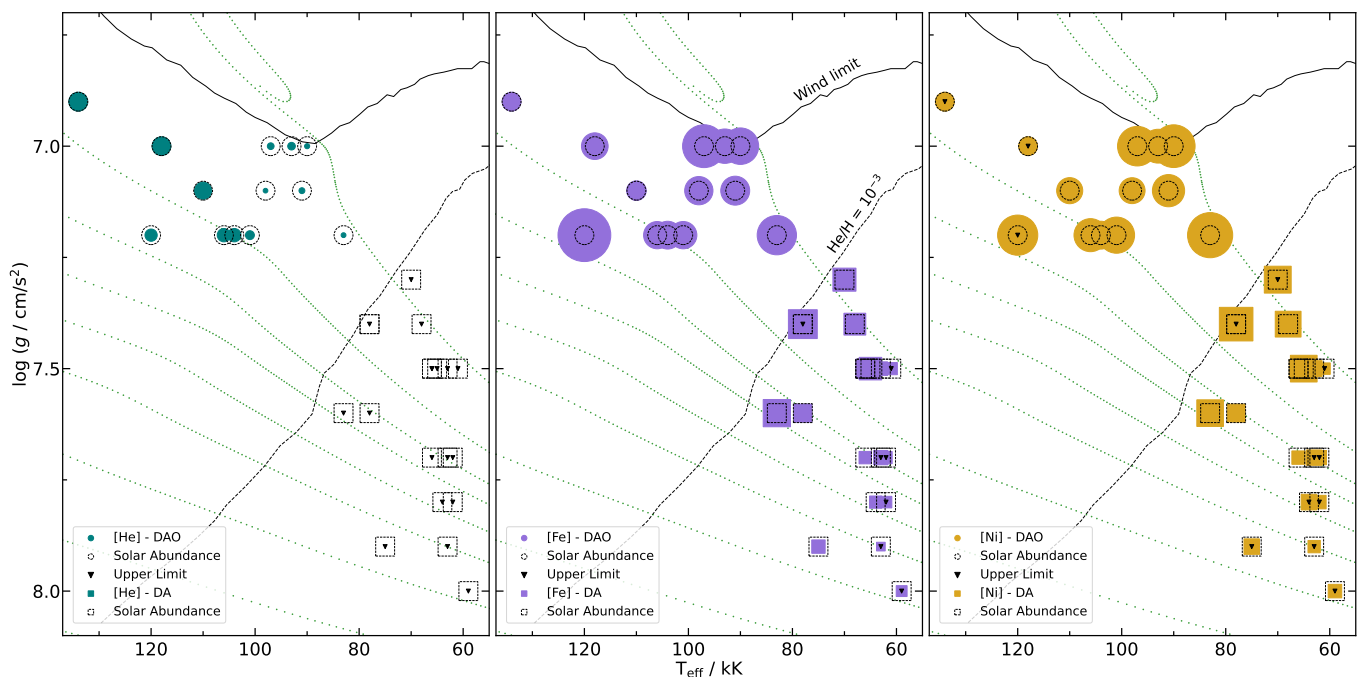


Fig. 10: Similar to Fig. 9, but for helium, iron, and nickel (from left to right).

plausible that the intense radiation pressure from the hot WDs in our sample ( $T_{\text{eff}} \geq 59$  kK) could halt the infall of the sublimated material, preventing the formation of even short-lived gaseous disks. Finally, it should be considered that the hot DA WD sample of Barstow et al. (2014) consisted of objects with lower  $T_{\text{eff}}$  (16–77 kK) than ours, and only  $\approx 20$  % of them exceed 50 kK. Although the observed Si abundance of a cool Hyades WD ( $T_{\text{eff}} \approx 20$  kK) can be explained with radiative levitation, for another object in the same cluster with a similar  $T_{\text{eff}}$ , accretion from external sources is needed (Chayer 2014). Therefore, the accretion-impacted abundance pattern of the DAs might only be a viable scenario for cooler objects (at about  $T_{\text{eff}} \leq 30$  kK).

In Sect. 3.2.2 we mentioned that it was not possible to fit all oxygen ions simultaneously in the DA WD spectra. When only O VI resonance lines are fit, the O abundance is far lower, and O IV and O V lines cannot be fit properly, and vice versa. It was suggested that inhomogeneous oxygen stratification causes this problem (Vennes et al. 2000; Vennes & Lanz 2001; Chayer et al. 2006; Rauch et al. 2013). By calculating self-consistent diffusion models, Rauch et al. (2013) showed that an improvement can be achieved when the O abundance is only decreased in the outer atmosphere, where the observed weak O VI resonance lines form. They suggested that a weak mass loss might diminish the O abundance in the outer atmosphere and might cause the observed O VI resonance line profiles.

However, chemically homogeneous line-driven winds are not expected above  $\log g = 7.0$  for a WD with  $T_{\text{eff}} = 60$  kK and (sub-) solar metallicity (Unglaub 2007). Fundamentally, abundance patterns of objects with similar parameters should be predicted by the equilibrium between gravitational settling and radiative levitation. Nonetheless, selective winds (or outflows) that only act on metal ions can still be expected (Babel 1995; Kr-tička et al. 2020) and influence the observed metal abundances. Unglaub (2007) showed that selective winds are predicted for the WDs ( $\log g \approx 7$ ) with mass-loss rate  $\dot{M} < 10^{-11} M_{\odot} \text{yr}^{-1}$ . Therefore, the discrepancy between observed abundances of DA WDs

and theoretical predictions might arise from the exclusion of mass loss in the diffusion calculations (Unglaub 2007, 2008).

## 5.2. Wind limit

Unglaub & Bues (2000) commented that if all WD progenitors had the same composition, they should be clearly separated in the Kiel diagram, and the previously observed coexistence of DAO and DA WDs in the same region can be explained by the difference in initial metallicity. A quick glance at Fig. 8 reveals otherwise: DAO and DA WDs are clearly separated in the Kiel diagram, and no DA resides above the predicted He abundance limit. Figs. 9 and 10 illustrate the metal abundances of individual objects in the Kiel diagram. In these plots, no substantial deviation in the abundances of DAOs and DAs among each other can be recognized. In comparison, the difference in the abundance pattern from one species to the next is conspicuous. In Fig. 10, the change in the He abundance in the Kiel diagram is depicted. When we accept that solar He abundance indicates a weak mass loss, our observational wind limit falls below the theoretical predictions. Around 105 kK, the decrease in He abundance can be observed. This was also reported by Werner et al. (2018b, 2019, 2020). All points above indicate that all hydrogen-rich WDs are born as DAOs and evolve into DAs. Therefore, the initial composition of our sample WDs probably does not substantially deviate in the objects, and the clear detachment of DAOs from DAs supports this claim. However, we should note that the termination point of mass loss probably differs for objects with different metallicities. Therefore, we speculate that finding DAOs far below the He limit, or vice versa for DAs, could be a direct indication of the difference in initial metallicity.

It is common practice to compile  $T_{\text{eff}}$  and  $\log g$  values from several studies for a broad overview of the evolutionary state of the WDs (Napiwotzki 1999; Unglaub & Bues 1998, 2000). However, it should be noted that the compiled studies might employ different stellar atmosphere codes and atomic data. Even minor deviations between codes can have a severe impact on the results,

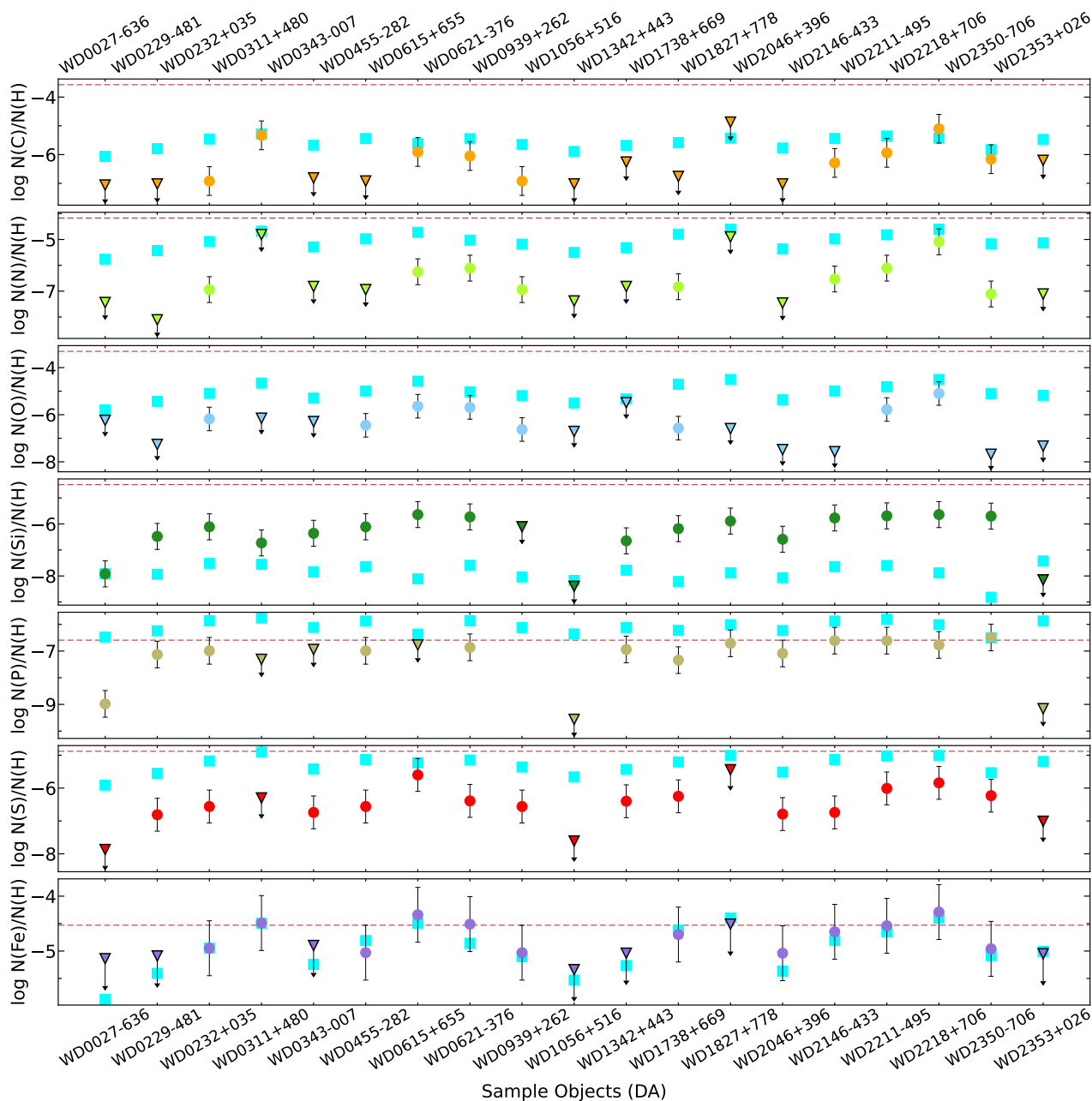


Fig. 11: Comparison of the C, N, O, Si, S, and Fe abundances (from top to bottom) in our DAs with predictions of diffusion theory by Chayer et al. (1995b) and for P by Vennes et al. (1996). The predictions are represented by turquoise squares. The solar abundances are indicated by horizontal dashed lines. The upper limits are marked with triangles.

as shown by Rauch (2008), who reported an (E)UV flux difference between models calculated with TMAP and TLUSTY<sup>7</sup> due to different cutoff frequencies of the H  $\gamma$  Lyman bound-free opacity. Therefore, conducting a homogeneous spectral analysis with the same code and atomic data is a key factor in our results. Even though other homogeneously performed analyses identified a tendency for DAOs to be hotter than DAs, a partial overlap of DAs and DAOs in the Kiel diagram persisted (Gianninas et al. 2010, 2011; Bédard et al. 2020). A result similar to ours can be observed in the  $T_{\text{eff}} - \log g$  diagram by Reindl et al. (2023), although several DA WDs inhabit a region slightly beyond the predicted He limit (see their Fig. 6). In all of these cases, the missing ingredient probably is the UV spectroscopy, which en-

<sup>7</sup> <http://nova.astro.umd.edu>

ables the inclusion of metal opacities in the model atoms and consequently paves the way to accurately assess  $T_{\text{eff}}$  by exploiting the ionization balance of metal lines.

### 5.3. Balmer-line problem

The occurrence of the BLP in a large fraction of DAO WDs has already been reported (Bergeron et al. 1994; Napiwotzki 1999; Gianninas et al. 2010; Bédard et al. 2020; Reindl et al. 2023), and the severity of this problem was tied to the high metal abundance by qualitatively comparing UV spectra of DAO and DA WDs (Gianninas et al. 2010). To evaluate the impact of the metallicity on the Balmer lines and the BLP, we calculated a set of models with finally adopted parameters that only included H and H+He

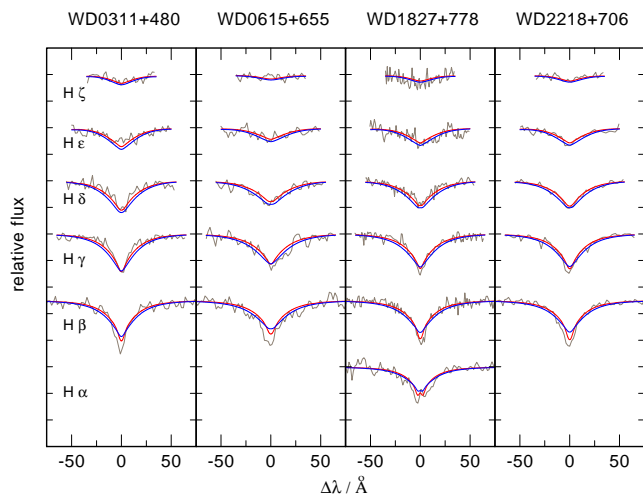


Fig. 12: Balmer lines (gray) of the DA WDs compared to the final model, including metal opacities (red) and pure H models (blue).

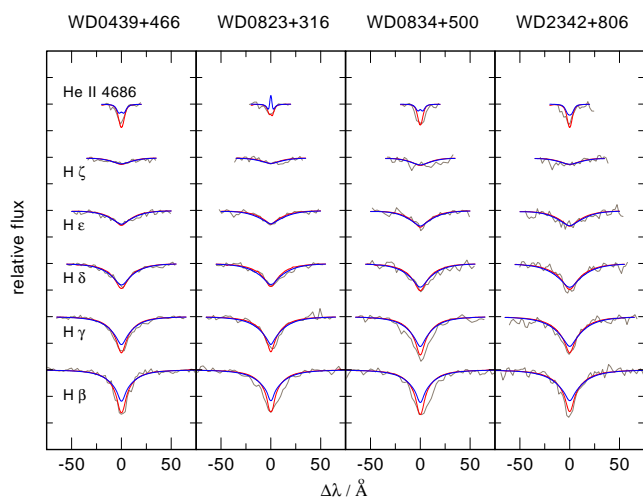


Fig. 13: He II and Balmer lines (gray) of the DAO WDs compared to the final model, including metal opacities (red) and H+He models (blue).

in the model atoms for DA and DAOs, respectively. With this configuration, we achieved satisfactory fits within the error range for 13 DA WDs. For the remaining 6 DAs, the BLP is more or less apparent with pure H models (Fig. 12). Notably, the latter 6 have a higher metal abundance than the rest of the DA WDs in our sample. Implementing a similar approach for DAOs yielded insufficient fits to He II  $\lambda$  4686 Å and Balmer lines without exception (Fig. 13). Although we did not try to achieve good fits with this configuration, a tendency for lower  $T_{\text{eff}}$  can be expected with H+He models. This might explain the large disparity in  $T_{\text{eff}}$  (up to 40 kK and 20 kK for DAOs and DAs, respectively) and  $\log g$  between previous optical studies and ours. However, a large discrepancy in  $T_{\text{eff}}$  compared to optical results by Gianninas et al. (2010, 2011) is still observed (Fig. 14), even though their models include (solar) C, N, and O opacities. While for DAOs, our models systematically predict higher  $T_{\text{eff}}$ , a general trend for DAs is not apparent.

Considering our models with finally accepted  $T_{\text{eff}}$ ,  $\log g$  and meticulously derived metal abundances from UV, we did not encounter severe cases of the BLP in our sample, except for two

DAOs (Fig. 13; WD 0823+316 and WD 0834+500) and two DA WDs (Fig. 12; WD 0311+480 and WD 0615+655), which respectively showed broader and deeper H $\beta$  than our models predict. However, the issues observed in the last four cases might depend on several factors, for instance, the data quality, data reduction, and normalization of the spectra. On the other hand, the data quality is of critical importance in detecting the BLP, as already remarked by Bédard et al. (2020) and Reindl et al. (2023). A high fraction of MWDD spectra in our sample have a reasonably high S/N ( $\approx 50$ ), but most of the observations do not contain the H $\alpha$  region. Additionally, the NLTE line-core emissions are not resolved because of the low resolution, which acts as a proxy for  $T_{\text{eff}}$ . Reindl et al. (2023) noted that they encountered the BLP more often in the higher-quality X-shooter data than in those from the Intermediate Dispersion Spectrograph (IDS) at the Isaac Newton Telescope (INT). The same outcome was also reported by Werner et al. (2018b) in the case of EGB6, for which the BLP was undetected in the low-resolution MWDD spectra (Gianninas et al. 2010). In contrast, the BLP still manifests in low-resolution, low S/N spectra even when the model atmosphere contains metal opacities (Werner et al. 2019). Therefore, our low-rate detection of BLP does not build a clear case for the solution being the inclusion of metals, but metals rather present an improvement to the results.

Finally, we would like to comment on the observed differences in  $\log g$  inferred from the Lyman and Balmer lines. We achieved satisfactory fits to the Lyman lines of WD 0621–373 and WD 2211–495 (see Fig. 2 as an example). However, H $\alpha$  and H $\beta$  cannot be reproduced properly with the same parameters, and a rather large decrease in  $\log g$  (0.3–0.4 dex) is needed, while the higher-order Balmer-line series agree. Both problematic objects have UVES and MWDD spectra, and the same effect can be observed in both datasets. A similar effect but in a more severe form has already been reported, where large scatter between UV and optical parameters is noticeable (Barstow et al. 2003b; Good et al. 2004). For objects above 50 kK, Vennes et al. (2005) showed that  $T_{\text{eff}}$  measured from Lyman lines exceeds up to  $\approx 15\%$ . However, they demonstrated that when heavy elements are included in the model calculations, a decrease of up to 16 kK in the Lyman-line temperature could be expected. Their sample also included WD 0621–373 and WD 2211–495, and for both objects, they derived  $T_{\text{eff}} > 70$  kK and  $\approx 65$  kK with pure H models from UV and optical spectra, respectively. Both of their Lyman-line temperatures are above our error limit, and their  $\log g$  values from UV are lower, but consistent with ours within the uncertainty. Our case demonstrates that with the inclusion of metals and employing ionization equilibria, a common ground for  $T_{\text{eff}}$  can be found for both wavelength regimes. Since the temperature is fixed, our results from different bands do not substantially deviate from one another in general, as opposed to previous studies. In the case of problematic objects, another factor should perhaps be considered (e.g., data reduction or normalization).

## 6. Summary and conclusion

We analyzed a sample of 19 DA and 13 DAO WDs, which have  $T_{\text{eff}} > 60$  kK and for which UV spectra are available, using state-of-the-art metal-line blanketed NLTE model atmospheres to extract crucial information about the spectral evolution of hot H-rich WDs. The effective temperatures and gravities were derived accurately by exploiting the ionization balances of the metal lines in the UV spectra. The abundances of helium and metals

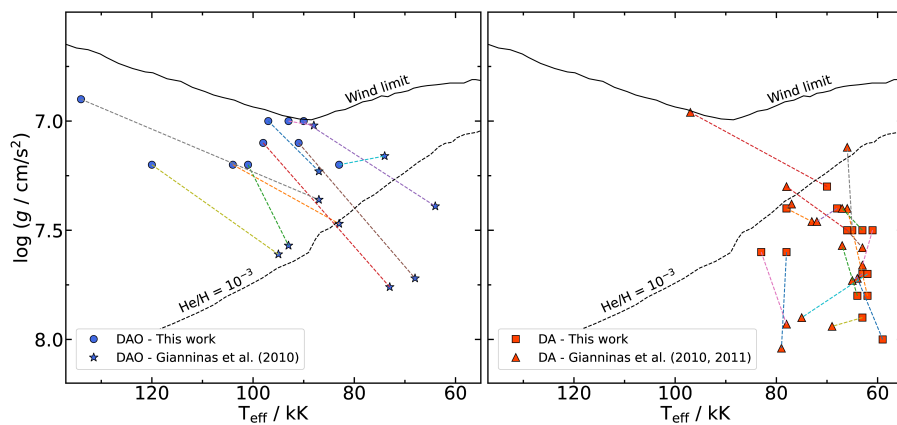


**Fig. 14.**  $T_{\text{eff}}$  and  $\log g$  values of the sample objects (DAO shown as blue circles, and DA shown as red squares) compared to the optical results (DAO shown as blue stars, and DA shown as red triangles) by [Gianninas et al. \(2010, 2011\)](#).

were measured with high accuracy. Our main results are listed below.

(i) In contrast to earlier studies, we find a clear separation of DAs and DAOs in the Kiel diagram (Fig. 8). Hydrogen-rich WDs are born as DAOs and turn into DAs when they cool to  $T_{\text{eff}} \approx 75\text{--}85$  kK. At around this temperature, helium becomes depleted by gravitational settling, as predicted by the combined theory of diffusion and mass loss.

(ii) In agreement with theory, we witness a gradual decrease in the helium abundance when DAOs cool (Fig. 10). The abundances of CNO elements also decrease, but less rapidly, again in accordance with theory (Fig. 9). Other light metals (Si, P, and S) follow a similar trend (Fig. 9).

(iii) According to the He abundance pattern of DAOs, the observational wind limit is slightly shifted downward in the Kiel diagram compared to the theoretical predictions (Fig. 10).

(iv) As DAOs approach the transformation into DAs, an increase in the iron and nickel abundances is observed (Fig. 10). Along with the decrease in the abundance of other elements, this indicates that mass loss can no longer efficiently homogenize the atmosphere.

(v) Diffusion theory assuming equilibrium of radiative acceleration and gravity generally fails to explain the observed metal abundances in hot DAs. This has been stated in many earlier works. However, we report clear systematic trends in our homogeneous sample. For virtually all DAs in our sample, theory overpredicts the abundances of C, N, O, P, and S, but underpredicts the abundance of Si (Fig. 11). Theory and observation agree for iron. The causes of the discrepancies remain unclear, but, as reasoned before by others, residual weak mass loss might be the cause.

(vi) There is no indication that the accretion of circumstellar material is relevant in our sample. All DAs have a similar metal abundance pattern.

(vii) The Balmer-line problem in DAOs is mitigated by the inclusion of metals with abundances determined from the UV analyses, but it does not disappear.

(viii) In contrast to earlier work, we generally encountered no large discrepancies between Balmer- and Lyman-line fits; hence, we find no indication of problems with the line-broadening theory. Larger deviations in gravity determinations are detected for a few objects, but this may be introduced by uncertainties in data reduction and normalization of the optical spectra or by strong ISM line blending in the case of UV spectra.

In conclusion, we emphasize that UV spectroscopy is the key to a reliable parameter determination of hot hydrogen-rich WDs and, hence, their spectral evolution.

Data availability. The model fits to the UV and optical spectra of the sample objects as well as the comparison of  $T_{\text{eff}}$ ,  $\log g$ , and abundances to previous studies are available at <https://doi.org/10.5281/zenodo.13940390> as online supplementary material.

*Acknowledgements.* We thank the referee for a constructive report that helped to improve the paper. We also thank Simon Preval and Martin Barstow for sending us the STIS spectrum of WD0455-282. S.F. is supported by the Deutsche Forschungsgemeinschaft (grant WE1312/58-1). N.R. is supported by the Deutsche Forschungsgemeinschaft (DFG) through grant RE3915/2-1. The TMAD (<http://astro.uni-tuebingen.de/~TMAD>) and TIRO tool (<http://astro.uni-tuebingen.de/~TIRO>) used for this paper was constructed as part of the activities of the German Astrophysical Virtual Observatory. Some of the data presented in this paper were obtained from the Mikulski Archive for Space Telescopes (MAST). This work is based on observations made with the NASA/ESA *Hubble* Space Telescope obtained from the Space Telescope Science Institute (STScI), which is operated by the Association of Universities for Research in Astronomy, Inc., under NASA contract NAS 5-26555. Funding for the SDSS and SDSS-II has been provided by the Alfred P. Sloan Foundation, the Participating Institutions, the National Science Foundation, the U.S. Department of Energy, the National Aeronautics and Space Administration, the Japanese Monbukagakusho, the Max Planck Society, and the Higher Education Funding Council for England. The SDSS Web Site is <http://www.sdss.org/>. This work is based on data obtained from the ESO Science Archive Facility. This research has made use of NASA's Astrophysics Data System and the SIMBAD database, operated at CDS, Strasbourg, France. This research has made use of the VizieR catalogue access tool, CDS, Strasbourg, France. This research made use of TOPCAT, an interactive graphical viewer and editor for tabular data ([Taylor 2005](http://www.starlink.org/~topcat/)).

## References

- Abazajian, K. N., Adelman-McCarthy, J. K., Agüeros, M. A., et al. 2009, *ApJS*, 182, 543
- Adamczak, J., Werner, K., Rauch, T., et al. 2012, *A&A*, 546, A1
- Asplund, M., Grevesse, N., Sauval, A. J., & Scott, P. 2009, *ARA&A*, 47, 481
- Babel, J. 1995, *A&A*, 301, 823
- Barstow, M. A., Bannister, N. P., Holberg, J. B., et al. 2001a, *MNRAS*, 325, 1149
- Barstow, M. A., Barstow, J. K., Casewell, S. L., Holberg, J. B., & Hubeny, I. 2014, *MNRAS*, 440, 1607
- Barstow, M. A., Bond, H. E., Burleigh, M. R., & Holberg, J. B. 2001b, *MNRAS*, 322, 891
- Barstow, M. A., Good, S. A., Burleigh, M. R., et al. 2003a, *MNRAS*, 344, 562
- Barstow, M. A., Good, S. A., Holberg, J. B., et al. 2002, *MNRAS*, 330, 425
- Barstow, M. A., Good, S. A., Holberg, J. B., et al. 2003b, *MNRAS*, 341, 870
- Barstow, M. A., Holberg, J. B., Fleming, T. A., et al. 1994, *MNRAS*, 270, 499
- Barstow, M. A., Hubeny, I., & Holberg, J. B. 1998, *MNRAS*, 299, 520
- Bédard, A. 2024, *Ap&SS*, 369, 43
- Bédard, A., Bergeron, P., Brassard, P., & Fontaine, G. 2020, *ApJ*, 901, 93
- Bédard, A., Bergeron, P., & Fontaine, G. 2017, *ApJ*, 848, 11
- Bédard, A., Brassard, P., Bergeron, P., & Blouin, S. 2022, *ApJ*, 927, 128
- Bergeron, P., Wesemael, F., Beauchamp, A., et al. 1994, *ApJ*, 432, 305
- Bergeron, P., Wesemael, F., Fontaine, G., et al. 2021, *AJ*, 162, 188
- Blöcker, T., Herwig, F., Driebe, T., Bramkamp, H., & Schönberner, D. 1997, in *Astrophysics and Space Science Library*, Vol. 214, White dwarfs, ed. J. Isern, M. Hernanz, & E. Garcia-Berro, 57

- Bragaglia, A., Renzini, A., & Bergeron, P. 1995, *ApJ*, 443, 735
- Chayer, P. 2014, *MNRAS*, 437, L95
- Chayer, P., Fontaine, G., & Pelletier, C. 1997, in *Astrophysics and Space Science Library*, Vol. 214, White dwarfs, ed. J. Isern, M. Hernanz, & E. Garcia-Berro, 253
- Chayer, P., Fontaine, G., & Wesemael, F. 1995a, *ApJS*, 99, 189
- Chayer, P., Oliveira, C., Dupuis, J., Moos, H. W., & Welsh, B. Y. 2006, in *Astronomical Society of the Pacific Conference Series*, Vol. 348, *Astrophysics in the Far Ultraviolet: Five Years of Discovery with FUSE*, ed. G. Sonneborn, H. W. Moos, & B. G. Andersson, 209
- Chayer, P., Vennes, S., Pradhan, A. K., et al. 1995b, *ApJ*, 454, 429
- Cunningham, T., Wheatley, P. J., Tremblay, P.-E., et al. 2022, *Nature*, 602, 219
- Delgado Inglada, G., Rodríguez, M., Mampaso, A., & Viironen, K. 2009, *ApJ*, 694, 1335
- Dobbie, P. D., Barstow, M. A., Hubeny, I., et al. 2005, *MNRAS*, 363, 763
- Dufour, P., Blouin, S., Coutu, S., et al. 2017, in *Astronomical Society of the Pacific Conference Series*, Vol. 509, 20th European White Dwarf Workshop, ed. P. E. Tremblay, B. Gänsicke, & T. Marsh, 3
- Finley, D. S., Koester, D., & Basri, G. 1997, *ApJ*, 488, 375
- Fitzpatrick, E. L. 1999, *PASP*, 111, 63
- Frew, D. J. 2008, PhD thesis, Macquarie University, Department of Physics and Astronomy
- Frew, D. J. & Parker, Q. A. 2010, *PASA*, 27, 129
- Frew, D. J., Parker, Q. A., & Bojičić, I. S. 2016, *MNRAS*, 455, 1459
- Gänsicke, B. T., Schreiber, M. R., Toloza, O., et al. 2019, *Nature*, 576, 61
- Gentile Fusillo, N. P., Manser, C. J., Gänsicke, B. T., et al. 2021a, *MNRAS*, 504, 2707
- Gentile Fusillo, N. P., Tremblay, P. E., Cukanovaite, E., et al. 2021b, *MNRAS*, 508, 3877
- Gianninas, A., Bergeron, P., Dupuis, J., & Ruiz, M. T. 2010, *ApJ*, 720, 581
- Gianninas, A., Bergeron, P., & Ruiz, M. T. 2011, *ApJ*, 743, 138
- Good, S. A., Barstow, M. A., Burleigh, M. R., Dobbie, P. D., & Holberg, J. B. 2005a, *MNRAS*, 364, 1082
- Good, S. A., Barstow, M. A., Burleigh, M. R., et al. 2005b, *MNRAS*, 363, 183
- Good, S. A., Barstow, M. A., Holberg, J. B., et al. 2004, *MNRAS*, 355, 1031
- Greenstein, J. L. & Eggen, O. J. 1966, *Vistas in Astronomy*, 8, 63
- Guo, J., Zhao, J., Tziamtzis, A., et al. 2015, *MNRAS*, 454, 2787
- Hall, P. D., Tout, C. A., Izzard, R. G., & Keller, D. 2013, *MNRAS*, 435, 2048
- Hébrard, G., Friedman, S. D., Kruk, J. W., et al. 2002, *Planet. Space Sci.*, 50, 1169
- Hébrard, G. & Moos, H. W. 2003, *ApJ*, 599, 297
- Henry, R. B. C., Kwitter, K. B., & Balick, B. 2004, *AJ*, 127, 2284
- Herald, J. E. & Bianchi, L. 2004, *PASP*, 116, 391
- Holberg, J. B., Barstow, M. A., Buckley, D. A. H., et al. 1993, *ApJ*, 416, 806
- Holberg, J. B., Wesemael, F., & Basile, J. 1986, *ApJ*, 306, 629
- Homeier, D., Koester, D., Hagen, H. J., et al. 1998, *A&A*, 338, 563
- Hu, J., Webb, J. K., Ayres, T. R., et al. 2021, *MNRAS*, 500, 1466
- Joyce, S. R. G., Barstow, M. A., Casewell, S. L., et al. 2018, *MNRAS*, 479, 1612
- Jura, M. 2003, *ApJ*, 584, L91
- Kawka, A., Vennes, S., Schmidt, G. D., Wickramasinghe, D. T., & Koch, R. 2007, *ApJ*, 654, 499
- Kepler, S. O., Koester, D., Pelisoli, I., Romero, A. D., & Ourique, G. 2021, *MNRAS*, 507, 4646
- Kepler, S. O., Pelisoli, I., Koester, D., et al. 2019, *MNRAS*, 486, 2169
- Koester, D., Gänsicke, B. T., & Farihi, J. 2014, *A&A*, 566, A34
- Koester, D., Liebert, J., & Hege, E. K. 1979, *A&A*, 71, 163
- Koester, D., Napiwotzki, R., Christlieb, N., et al. 2001, *A&A*, 378, 556
- Koester, D., Rollenhagen, K., Napiwotzki, R., et al. 2005, *A&A*, 432, 1025
- Koester, D., Voss, B., Napiwotzki, R., et al. 2009, *A&A*, 505, 441
- Krtićka, J., Kubát, J., & Krtićková, I. 2020, *A&A*, 635, A173
- Lajoie, C. P. & Bergeron, P. 2007, *ApJ*, 667, 1126
- Lamberts, A., Blunt, S., Littenberg, T. B., et al. 2019, *MNRAS*, 490, 5888
- Lei, Z., He, R., Németh, P., et al. 2023, *ApJ*, 942, 109
- Lemoine, M., Vidal-Madjar, A., Hébrard, G., et al. 2002, *ApJS*, 140, 67
- Lépine, S., Bergeron, P., & Lanning, H. H. 2011, *AJ*, 141, 96
- Liebert, J., Bergeron, P., & Holberg, J. B. 2005, *ApJS*, 156, 47
- Limoges, M. M. & Bergeron, P. 2010, *ApJ*, 714, 1037
- Löbbling, L., Maney, M. A., Rauch, T., et al. 2020, *MNRAS*, 492, 528
- Madsen, G. J., Frew, D. J., Parker, Q. A., Reynolds, R. J., & Haffner, L. M. 2006, in *Planetary Nebulae in our Galaxy and Beyond*, ed. M. J. Barlow & R. H. Méndez, Vol. 234, 455–456
- Manseau, P. M., Bergeron, P., & Green, E. M. 2016, *ApJ*, 833, 127
- Manser, C. J., Gänsicke, B. T., Eggl, S., et al. 2019, *Science*, 364, 66
- Manser, C. J., Gänsicke, B. T., Gentile Fusillo, N. P., et al. 2020, *MNRAS*, 493, 2127
- Manser, C. J., Gänsicke, B. T., Marsh, T. R., et al. 2016, *MNRAS*, 455, 4467
- Marsh, M. C., Barstow, M. A., Buckley, D. A., et al. 1997, *MNRAS*, 286, 369
- McCarthy, J. K., Mendez, R. H., & Kudritzki, R. P. 1997, in *Planetary Nebulae*, ed. H. J. Habing & H. J. G. L. M. Lamers, Vol. 180, 120
- McCook, G. P. & Sion, E. M. 1999, *ApJS*, 121, 1
- Melis, C., Klein, B., Doyle, A. E., et al. 2020, *ApJ*, 905, 56
- Mendez, R. H., Kudritzki, R. P., Gruschinske, J., & Simon, K. P. 1981, *A&A*, 101, 323
- Mendez, R. H., Kudritzki, R. P., Herrero, A., Husfeld, D., & Groth, H. G. 1988, *A&A*, 190, 113
- Mendez, R. H., Kudritzki, R. P., & Simon, K. P. 1985, *A&A*, 142, 289
- Miller Bertolami, M. M. 2016, *A&A*, 588, A25
- Müller-Ringat, E. M. 2013, PhD thesis, Eberhard Karls University of Tübingen, Germany
- Napiwotzki, R. 1999, *A&A*, 350, 101
- Napiwotzki, R. & Schonberner, D. 1993, in *Planetary Nebulae*, ed. R. Weinberger & A. Acker, Vol. 155, 495
- Preval, S. P., Barstow, M. A., Bainbridge, M., et al. 2019, *MNRAS*, 487, 3470
- Ransom, R. R., Kothes, R., Geisbuesch, J., Reich, W., & Landecker, T. L. 2015, *ApJ*, 799, 198
- Rauch, T. 2008, *A&A*, 481, 807
- Rauch, T. & Deetjen, J. L. 2003, in *Astronomical Society of the Pacific Conference Series*, Vol. 288, *Stellar Atmosphere Modeling*, ed. I. Hubeny, D. Mihalas, & K. Werner, 103
- Rauch, T., Gamrath, S., Quinet, P., et al. 2020, *A&A*, 637, A4
- Rauch, T., Gamrath, S., Quinet, P., et al. 2017a, *A&A*, 599, A142
- Rauch, T., Hoyer, D., Quinet, P., Gallardo, M., & Raineri, M. 2015a, *A&A*, 577, A88
- Rauch, T., Quinet, P., Hoyer, D., et al. 2016a, *A&A*, 587, A39
- Rauch, T., Quinet, P., Hoyer, D., et al. 2016b, *A&A*, 590, A128
- Rauch, T., Quinet, P., Knörzer, M., et al. 2017b, *A&A*, 606, A105
- Rauch, T., Werner, K., Biémont, E., Quinet, P., & Kruk, J. W. 2012, *A&A*, 546, A55
- Rauch, T., Werner, K., Bohlin, R., & Kruk, J. W. 2013, *A&A*, 560, A106
- Rauch, T., Werner, K., Quinet, P., & Kruk, J. W. 2014a, *A&A*, 564, A41
- Rauch, T., Werner, K., Quinet, P., & Kruk, J. W. 2014b, *A&A*, 566, A10
- Rauch, T., Werner, K., Quinet, P., & Kruk, J. W. 2015b, *A&A*, 577, A6
- Rauch, T., Ziegler, M., Werner, K., et al. 2007, *A&A*, 470, 317
- Reindl, N., Bainbridge, M., Przybilla, N., et al. 2019, *MNRAS*, 482, L93
- Reindl, N., Islami, R., Werner, K., et al. 2023, *A&A*, 677, A29
- Renedo, I., Althaus, L. G., Miller Bertolami, M. M., et al. 2010, *ApJ*, 717, 183
- Schoening, T. & Butler, K. 1989, *A&AS*, 78, 51
- Schuh, S. L., Dreizler, S., & Wolff, B. 2002, *A&A*, 382, 164
- Stanghellini, L., Guerrero, M. A., Cunha, K., Machado, A., & Villaver, E. 2006, *ApJ*, 651, 898
- Taylor, M. B. 2005, in *Astronomical Society of the Pacific Conference Series*, Vol. 347, *Astronomical Data Analysis Software and Systems XIV*, ed. P. Shopbell, M. Britton, & R. Ebert, 29
- Traulsen, I., Hoffmann, A. I. D., Rauch, T., et al. 2005, in *Astronomical Society of the Pacific Conference Series*, Vol. 334, 14th European Workshop on White Dwarfs, ed. D. Koester & S. Moehler, 325
- Tremblay, P. E. & Bergeron, P. 2009, *ApJ*, 696, 1755
- Tremblay, P. E., Bergeron, P., & Gianninas, A. 2011, *ApJ*, 730, 128
- Tremblay, P. E., Cukanovaite, E., Gentile Fusillo, N. P., Cunningham, T., & Hollands, M. A. 2019, *MNRAS*, 482, 5222
- Tweedy, R. W. & Napiwotzki, R. 1994, *AJ*, 108, 978
- Unglaub, K. 2007, in *Astronomical Society of the Pacific Conference Series*, Vol. 372, 15th European Workshop on White Dwarfs, ed. R. Napiwotzki & M. R. Burleigh, 201
- Unglaub, K. 2008, *A&A*, 486, 923
- Unglaub, K. & Bues, I. 1998, *A&A*, 338, 75
- Unglaub, K. & Bues, I. 2000, *A&A*, 359, 1042
- Vennes, S. 1992, *ApJ*, 390, 590
- Vennes, S., Chayer, P., Dupuis, J., & Lanz, T. 2005, in *Astronomical Society of the Pacific Conference Series*, Vol. 334, 14th European Workshop on White Dwarfs, ed. D. Koester & S. Moehler, 185
- Vennes, S., Chayer, P., Fontaine, G., & Wesemael, F. 1989, *ApJ*, 336, L25
- Vennes, S., Chayer, P., Hurwitz, M., & Bowyer, S. 1996, *ApJ*, 468, 898
- Vennes, S., Chayer, P., Thorstensen, J. R., Bowyer, S., & Shipman, H. L. 1992, *ApJ*, 392, L27
- Vennes, S. & Fontaine, G. 1992, *ApJ*, 401, 288
- Vennes, S. & Lanz, T. 2001, *ApJ*, 553, 399
- Vennes, S., Pelletier, C., Fontaine, G., & Wesemael, F. 1988, *ApJ*, 331, 876
- Vennes, S., Polomski, E. F., Lanz, T., et al. 2000, *ApJ*, 544, 423
- Vennes, S., Thejll, P. A., Génova Galvan, R., & Dupuis, J. 1997, *ApJ*, 480, 714
- von Hippel, T., Kuchner, M. J., Kilic, M., Mullally, F., & Reach, W. T. 2007, *ApJ*, 662, 544
- Werner, K. 1996, *ApJ*, 457, L39
- Werner, K., Deetjen, J. L., Dreizler, S., et al. 2003, in *Astronomical Society of the Pacific Conference Series*, Vol. 288, *Stellar Atmosphere Modeling*, ed. I. Hubeny, D. Mihalas, & K. Werner, 31
- Werner, K. & Dreizler, S. 1999, *Journal of Computational and Applied Mathematics*, 109, 65
- Werner, K., Dreizler, S., Heber, U., et al. 1995, *A&A*, 293, L75
- Werner, K., Dreizler, S., & Rauch, T. 2012, TMAP: Tübingen NLTE Model-Atmosphere Package, *Astrophysics Source Code Library*, record ascl:1212.015
- Werner, K., Rauch, T., & Kruk, J. W. 2007, *A&A*, 466, 317
- Werner, K., Rauch, T., & Kruk, J. W. 2018a, *A&A*, 609, A107
- Werner, K., Rauch, T., & Kruk, J. W. 2018b, *A&A*, 616, A73
- Werner, K., Rauch, T., & Reindl, N. 2019, *MNRAS*, 483, 5291
- Werner, K., Reindl, N., Löbbling, L., et al. 2020, *A&A*, 642, A228
- Wesemael, F., Green, R. F., & Liebert, J. 1985, *ApJS*, 58, 379
- Wesemael, F., Henry, R. B. C., & Shipman, H. L. 1984, *ApJ*, 287, 868
- Ziegler, M. 2012, PhD thesis, Eberhard Karls University of Tübingen, Germany

## Appendix A: Remarks on individual objects

In this section we give a brief remark on each object and compare our spectroscopic results to previous analyses (Tables B.3 and B.4). If the same authors analyzed a particular object more than once, only the latest reported  $T_{\text{eff}}$  and  $\log g$  values were compared, excluding results acquired from a different waveband.

### A.1. DAO white dwarfs

**Longmore 1** For the central star of Longmore 1, we found  $T_{\text{eff}} = 118 \pm 5$  kK and  $\log g = 7.0 \pm 0.3$  which are in agreement with the values determined in other FUV analyses (Herald & Bianchi 2004; Ziegler 2012). This is the only object in our sample that shows C, N, and O enhancement (up to 1.1 dex). We determined solar He, P, S, Ni, and almost two times solar Fe abundances. All abundance measurements of Ziegler (2012) lie within our error limits except for N and Fe for which the discrepancy approaches  $\approx 1$  dex. Likewise, the abundance of several ions (C, N, Si) differs more than 0.5 dex from the results of Herald & Bianchi (2004). Additionally, multiple C IV, N IV, N V, O V, and O VI lines were identified in the UVES spectrum. Especially, O V and O VI lines in the optical range and NLTE-core emission of He II  $\lambda 4686$  Å and H $\alpha$  are extremely sensitive to temperature change, and our fit to the UVES spectrum affirms our measured parameters. Nonetheless, we achieved poor fits to H $\beta$ , H $\gamma$ , and He II  $\lambda 5412$  Å. This issue does not appear as a case of conventional Balmer-line problem since we achieve very good fits to He II  $\lambda 4686$  Å and H $\alpha$  as well as the higher order of Balmer-line series. Utilizing evolutionary tracks of Miller Bertolami (2016) revealed a post-AGB age of  $36 \pm 14$  kyr for the central star, which is consistent with the expected lifespan of PNe.

**WD 0439+466** is the DAO-type central star of the planetary nebula (PN) Sh 2-216. We estimate  $T_{\text{eff}} = 97 \pm 5$  kK and  $\log g = 7.0 \pm 0.2$ . Napiwotzki (1999) reports  $T_{\text{eff}} = 83.2 \pm 3.3$  kK and  $\log g = 6.74 \pm 0.19$  from their NLTE analysis of optical spectra consisting of H+He models. Another optical study by Gianninas et al. (2010) reached a similar conclusion for  $T_{\text{eff}}$  and  $\log g$  (87 kK, 7.23). The slight difference to our results can be attributed to the exclusion of metal opacities in the previous optical analyses. On the other hand, our results are in agreement with the values determined by Traulsen et al. (2005,  $T_{\text{eff}} = 93$  kK,  $\log g = 6.9$ ) and Rauch et al. (2007,  $T_{\text{eff}} = 95 \pm 2$  kK,  $\log g = 6.9 \pm 0.2$ ), who employed HST and FUSE spectra. Our study indicates 0.9 dex sub-solar He abundance, whereas C and O are slightly sub-solar, and N is solar. In contrast to light metals, we found Fe and Ni enhancement for this object (0.6–0.7 dex). Traulsen et al. (2005) derived abundances only for He, C, N, O, and Si. Among these ions, only N abundance substantially differs from our results. Also, our abundances agree very well with those from Rauch et al. (2007), the largest difference being less than 0.4 dex for Si.

**WD 0500–156** Optical and UV spectra of the DAO-type central star of PN Abell 7 were investigated multiple times since it has been analyzed by Mendez et al. (1981,  $T_{\text{eff}} = 75 \pm 10$  kK,  $\log g = 7.0 \pm 0.5$ ). Earlier optical studies with LTE and NLTE models reported a wide  $T_{\text{eff}}$  (60–100 kK) and  $\log g$  (6.60–7.47) range (Wesemael et al. 1985; McCarthy et al. 1997; Napiwotzki 1999; Good et al. 2004; Gianninas et al. 2010). Although FUV analyses reach a smaller discrepancy in  $T_{\text{eff}}$  (99–109 kK), the  $\log g$  difference (7.00–7.68) remains large (Good et al. 2004; Ziegler 2012). From our FUV plus optical study, we determined  $T_{\text{eff}} = 104 \pm 6$  kK and  $\log g = 7.20 \pm 0.2$ . We found the

He abundance as half of the solar value. C and O abundances are around the solar value, whereas N is slightly depleted. Other light metals (Si, P, S) were also found as sub-solar, while Fe and Ni are lightly enhanced. In general, our abundances agree very well with other studies (Good et al. 2005b; Ziegler 2012); however, C and N abundances by Good et al. (2005b) reside slightly outside of our error limit.

**WD 0615+556** is the DAO-type central star of PN PuWe 1. We derived  $T_{\text{eff}} = 101 \pm 5$  kK and  $\log g = 7.2 \pm 0.2$ . In general,  $T_{\text{eff}}$  difference is less than 10 kK compared to previous optical or UV analyses (McCarthy et al. 1997; Napiwotzki 1999; Gianninas et al. 2010; Ziegler 2012) and only  $\log g$  value of Gianninas et al. (2010) and Good et al. (2004, from Lyman lines) lies 0.2 dex out of our error limit. We did not find an agreement with the optical study of (Good et al. 2004), estimating  $T_{\text{eff}} = 74.2 \pm 4.8$  kK,  $\log g = 7.02 \pm 0.20$ . He abundance was determined to be one-fifth of the solar value. We found that N, O, Si, and S are slightly depleted, whereas P, Fe, and Ni are 0.3 to 0.5 dex enhanced. An upper limit to C abundance can be assigned as the solar value. Abundance measurements of Ziegler (2012) are similar to ours, the only statistically significant difference being the P and S abundance. We find a larger disagreement with values from Good et al. (2005b), except for Ni abundance.

**WD 0823+316** is the DAO-type central star of PN TK 1. We estimate  $T_{\text{eff}} = 98 \pm 5$  kK and  $\log g = 7.1 \pm 0.2$ . The He abundance was derived as  $\log(\text{He}/\text{H}) = -2.41$ , one of the lowest in the sample. We found solar C and P abundances, N is slightly over-solar, and O is slightly sub-solar. Si and S are highly depleted. We encounter over-solar Fe and Ni abundances. Previous optical analyses of this object yielded lower  $T_{\text{eff}}$  values ranging from 64 kK to 79 kK (Bergeron et al. 1994; Good et al. 2004; Gianninas et al. 2010; Tremblay et al. 2011; Bédard et al. 2020). However, we found a perfect agreement with the only other UV analysis by Good et al. (2004,  $T_{\text{eff}} = 99 \pm 4$  kK,  $\log g = 7.26 \pm 0.07$ ). Our abundances also assent with Good et al. (2005b), except for C and O, which are  $\sim 6$  and 50 times less than ours.

**WD 0834+500** is the second coolest DAO-type WD in our sample with  $T_{\text{eff}} = 90 \pm 3$  kK,  $\log g = 7.0 \pm 0.2$  and  $\log(\text{He}/\text{H}) = -2.33$ . We achieved an excellent fit to the FUSE spectrum, resulting in slightly sub-solar to solar light metal and over-solar Fe and Ni abundances. In contrast to the FUV, our optical fits are not in perfect coherence for given parameters. The line core of H $\gamma$  is deeper, and the overall line strength is stronger than our model. On the other hand, our model gives a satisfactory fit to the line core of  $\beta$ , yet the equivalent width of the line is larger than the model predicts. However, higher orders of the Balmer-line series fit very well, indicating an accurate  $\log g$  measurement. Former optical studies indicate much lower  $T_{\text{eff}}$ , around 60 kK; in contrast,  $\log g$  values always reside within our error limits (Bergeron et al. 1994; Good et al. 2004; Gianninas et al. 2010). This is anticipated since not including metal opacities is compensated with a lower  $T_{\text{eff}}$ .

**WD 0851+090** We derived  $T_{\text{eff}} = 106 \pm 5$  kK,  $\log g = 7.2 \pm 0.2$  for the DAO-type central star of Abell 31. We encounter the same issue as with Longmore 1 in the UVES spectrum of Abell 31. All of the Balmer and He II line fits are satisfactory except for H $\gamma$  and He II  $\lambda 5412$  Å. We estimate the He abundance as half of the solar value. C, N, and O are determined as roughly solar, but Si and S are up to 0.7 dex sub-solar. In comparison, Fe and Ni are slightly enhanced. Our abundances match very well with Ziegler (2012), S and Fe being the only ions with a large discrepancy. While Good et al. (2005b) reported significantly (76 and 20 times) lower N and O content than ours, for other



elements, deviations are less than one dex. Additionally, previous studies largely deviate from one another regarding  $T_{\text{eff}}$  and  $\log g$ . On one hand, Balmer fits of Good et al. (2004) resulted in  $T_{\text{eff}} = 74.7 \pm 6.0$  kK,  $\log g = 9.95 \pm 0.15$ , on the other hand, Ziegler (2012) inferred  $T_{\text{eff}} = 114 \pm 10$  kK,  $\log g = 7.4 \pm 0.3$  from FUSE spectra.

**WD 1111+552** is the only object for which we did not have optical spectra. We only utilized FUSE observations of the DAO-type central star of PN M 97 (NGC 3587) and determined  $T_{\text{eff}} = 110 \pm 5$  kK and  $\log g = 7.1 \pm 0.3$ . Other than Si and S, which are 0.7 and 0.8 dex sub-solar, element abundances are derived as roughly solar. He, N, and O abundances agree well with the PN abundances derived by Stanghellini et al. (2006), but Fe, which is roughly two dex higher than inferred from PN by Delgado Inglada et al. (2009). While in general, these measurements, including  $T_{\text{eff}}$  and  $\log g$ , are in good agreement with Ziegler (2012), we estimate  $\approx 12$  times more N content. Furthermore,  $T_{\text{eff}}$  and  $\log g$  parameters are comparable to early optical analyses (McCarthy et al. 1997), with only Napiwotzki (1999) reporting a temperature 10 kK below our error range.

**WD 1214+267** is the third coolest DAO WD in our sample ( $T_{\text{eff}} = 91 \pm 3$  kK,  $\log g = 7.1 \pm 0.3$ ). While early optical studies reported 20 to 30 kK lower temperature and 0.5 to 0.6 dex higher surface gravity (Bergeron et al. 1994; Good et al. 2004; Gianninas et al. 2010), by fitting Lyman lines in the FUSE spectra, Good et al. (2004) conclude  $T_{\text{eff}} = 87.6 \pm 3.7$  kK,  $\log g = 6.96 \pm 0.04$ . Guo et al. (2015) derived  $T_{\text{eff}} = 80.3 \pm 4.9$  kK,  $\log g = 7.05 \pm 0.20$  by utilizing LAMOST spectra; however, they misclassified the object as DA WD. We estimate a roughly one dex sub-solar He abundance. All light metals are sub-solar, with S being the least abundant (one dex sub-solar) among them, whereas heavier elements are slightly enhanced. Good et al. (2005b) reported only C, O, Si, and Fe abundances. Among them, only O drastically differs from our measurements.

**WD 1253+378** Since it has been discovered (Koester et al. 1979), the prototype DAO WD HZ 34 was observed and analyzed multiple times, generating a wide parameter range for temperature (60–91 kK) and surface gravity (6.51–7.02) of the object (Wesemael et al. 1985; Bergeron et al. 1994; Napiwotzki 1999; Good et al. 2004; Gianninas et al. 2010). With  $T_{\text{eff}} = 93 \pm 4$  kK and  $\log g = 7.0 \pm 0.2$ , our results reside at the high end of this parameter range. Additionally, we found 0.7 dex sub-solar He abundance. While we measured slightly sub-solar C, O, and P abundances, N, Si, and S are 10 times sub-solar. On the other hand,  $\approx 0.5$  dex Fe and Ni enhancement was detected compared to the Sun. Besides He and Si, our abundances significantly differ than Good et al. (2005b).

**WD 1957+225** is the hottest DAO-type CSPN (NGC 6853) in our sample ( $T_{\text{eff}} = 134 \pm 10$  kK and  $\log g = 6.9 \pm 0.4$ ). We found roughly solar abundances for all elements except for Si, which is  $\approx 0.5$  dex sub-solar. PN abundances (He, N, and O) derived by Stanghellini et al. (2006) reside within our error range. In general, our  $T_{\text{eff}}$ ,  $\log g$  and abundance values are consistent with previous FUV analyses (Traulsen et al. 2005; Ziegler 2012), except for Fe abundance reported by Ziegler (2012) which is 1.5 dex sub-solar. However,  $T_{\text{eff}}$  and  $\log g$  parameters derived in optical analyses reveal notable differences. For instance, the disparity in  $T_{\text{eff}}$ , considering our lower limit, extends to  $\sim 15$  kK compared to Napiwotzki (1999,  $T_{\text{eff}} = 108.6 \pm 6.8$  kK  $\log g = 6.72 \pm 0.23$ ). The deviation is even larger in comparison to Gianninas et al. (2010,  $T_{\text{eff}} = 86.7 \pm 5.4$  kK,  $\log g = 7.36 \pm 0.18$ ). We encountered is-

ues fitting the Balmer lines, especially  $H\beta$ , which is significantly stronger than our models. However, we appoint this to over-correction of the spectrum during background subtraction because forbidden nebular lines (O[III]) are also in absorption instead of emission. This issue was also reported by Gianninas et al. (2010) and might be the reason for their significantly lower  $T_{\text{eff}}$ .

**WD 2226–210** is the central star of Helix nebula (NGC 7293). We derived  $T_{\text{eff}} = 120 \pm 5$  kK and  $\log g = 7.2 \pm 0.3$  and 0.4 dex sub-solar He abundance. O, Si, and S are slightly depleted, and other light metals are comparable to solar abundance. On the other hand, Fe and Ni are enriched by 0.9 and 0.7 dex super-solar, respectively. S abundance determined from PN by Henry et al. (2004) is in agreement with the photospheric abundances, whereas He, N, and O abundances lie 0.1 dex above our error limit. Aside from the substantial  $\log g$  difference (0.9 dex) with Traulsen et al. (2005), all parameters from other FUV analyses (Traulsen et al. 2005; Ziegler 2012) remain within our error range. While previous optical studies report lower  $T_{\text{eff}}$  in a consistent manner, ranging from 90 kK to 104 kK (Mendez et al. 1985, 1988; McCarthy et al. 1997; Napiwotzki 1999; Gianninas et al. 2010),  $\log g$  values differ significantly (6.6–7.6 dex).

**WD 2342+806** is the coolest ( $T_{\text{eff}} = 83 \pm 5$  kK,  $\log g = 7.2 \pm 0.2$ ) DAO-type WD (GD 561) with one of the lowest He content (1.2 dex sub-solar) in our sample. C, N, O, Si, and S abundances range between  $\sim 0.2$  to 0.5 dex sub-solar, whereas Fe and Ni are enriched up to 6 times the solar content. He, Si, P, and S abundances determined by Ziegler (2012) remain out of our error limits; other species agree. Except for Fe, our results are consistent with Good et al. (2005b). All previous studies report lower  $T_{\text{eff}}$  and  $\log g$  values than ours.

GD 561 was associated with PN Sh 2-174 (Napiwotzki & Schonberner 1993; Tweedy & Napiwotzki 1994). Bergeron et al. (1994) suggests that the spectroscopic parameters are consistent with a post-EHB star that did not go through the AGB phase. Napiwotzki (1999) argues that any ejected material on the red giant branch (RGB) would not persist due to long evolutionary time scales on the horizontal branch, and the mass of the remaining EHB star would be too low to create the associated nebula. Tweedy & Napiwotzki (1994) reports the possibility of GD 561 being a low-mass post-RGB object that was produced through binary interaction, which, in that case, makes Sh 2-174 the envelope lost in the common envelope evolution. However, the vast disparity between the kinematical age of the PN and the supposed post-RGB lifetime of the WD (Napiwotzki 1999) decreases the likelihood. Additionally, the common envelope evolution scenario requires presence of a companion. However, Good et al. (2005a) did not detect a statistically significant RV shift. Also, there is no infrared excess, indicating a close companion (Filiz et al. in prep.). Ransom et al. (2015) identifies the system as a PN-ISM interaction through their radio analysis. On the other hand, Madsen et al. (2006) reports the kinematics of the gas inferred from optical emission lines. Frew (2008) concluded that the determined nebular velocity is statistically different from the stellar velocity, and the presence of a strong bowshock is required if the associated star is co-moving with the PN. Instead, they suggested that Sh 2-174 is an HII region in the ambient ISM, mimicking a true PN (Frew & Parker 2010; Frew et al. 2016).

Our estimated mass from the Kiel diagram ( $0.53 \pm 0.04 M_{\odot}$ ) is higher than previous analyses and indicates that GD 561 is likely a post-AGB star. From the evolutionary tracks of Miller Bertolami (2016), we determined a post-AGB age of  $230 \pm$

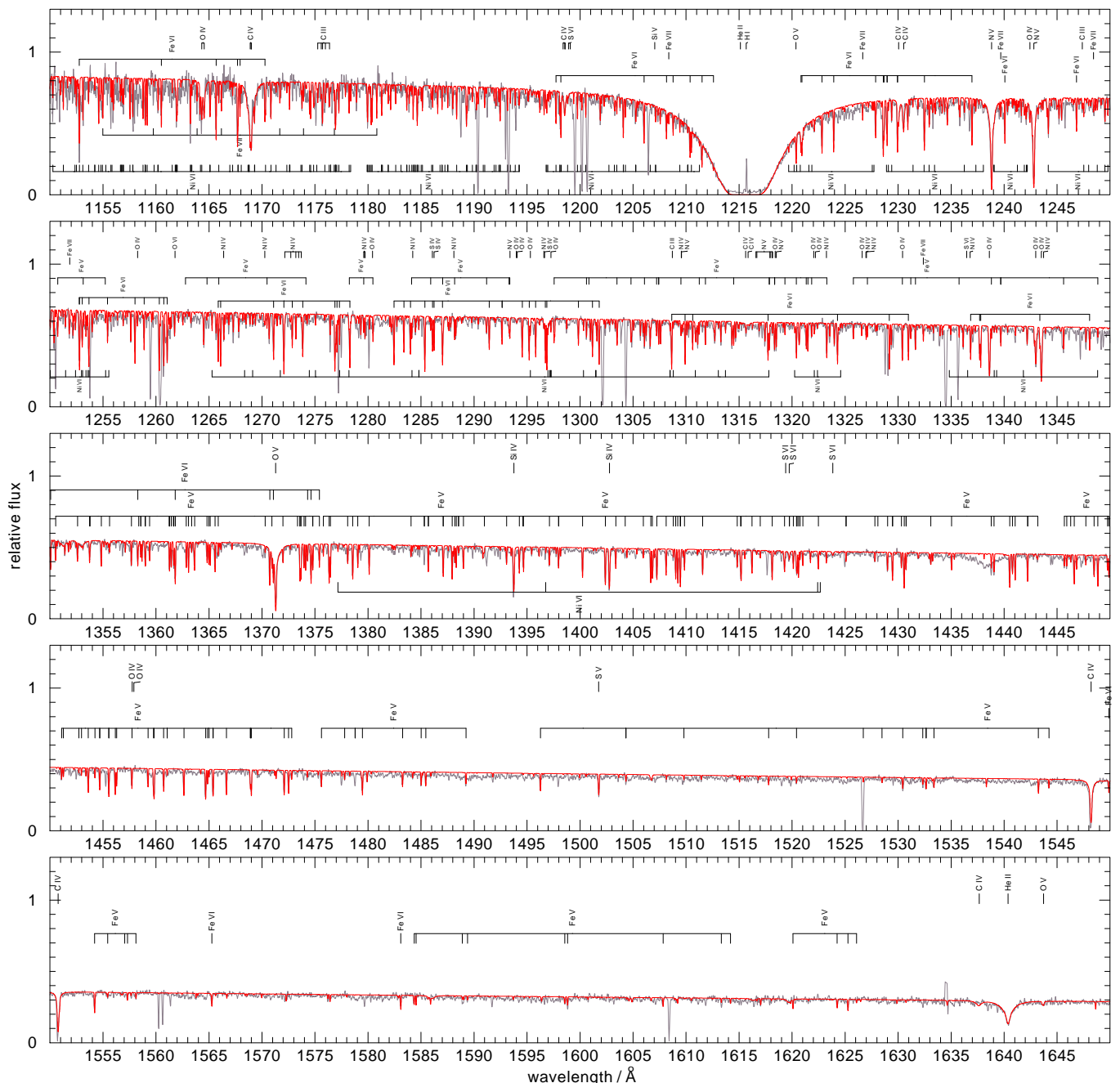


Fig. A.1: HST spectrum of the DAO WD 2342+806 (red: model with  $T_{\text{eff}} = 83$  kK,  $\log g = 7.2$ ).

73 kyr. Our estimated age of the WD is higher than the expected lifetime (10–100 kyr) of a bona fide PN. This agrees with Sh 2-174 being an HII region.

## A.2. DA white dwarfs

**WD 0027–636** is the coolest DA WD in our sample ( $T_{\text{eff}} = 59 \pm 5$  kK,  $\log g = 8.0 \pm 0.2$ ). The given parameters are in unison with former studies, and only  $\log g$  values determined by Vennes et al. (1997), Gianninas et al. (2011) and Bergeron et al. (2021) remain 0.2 dex out of our error range. All light metals are extremely sub-solar, whereas Fe and Ni are lightly depleted. Except for Si and P, we report upper-limit abundances. Only C, O, and Fe values are in agreement with the

diffusion calculations of Chayer et al. (1995b). To the best of our knowledge, no other abundance measurements have been reported for this object. In their FUV analysis, Barstow et al. (2014) only report  $T_{\text{eff}}$  and  $\log g$  values.

**WD 0229–481** We estimate  $T_{\text{eff}} = 62 \pm 5$  kK and  $\log g = 7.8 \pm 0.2$  for this DA WD. With CNO being highly depleted and given as upper limits, the abundance pattern shows a sub-solar content, though the P, Fe, and Ni deficit is about 0.4 dex. Only Fe and P abundances are comparable to theoretical calculations of Chayer et al. (1995b) and Vennes et al. (1996), respectively. Barstow et al. (2014) determined the C, Si, P, and S abundances of this object, and except for C, abundances lie within our error limits. Other than  $T_{\text{eff}}$  reported by Bragaglia et al. (1995) and Lajoie & Bergeron (2007), the highest temperature difference is 5 kK

in comparison to previous studies. However, we find larger discrepancies in surface gravity.

**WD 0232+035** Feige 24 is one of the most often analyzed hot-DA WDs with observations from EUV to infrared, of which binary nature has been long known (Greenstein & Eggen 1966). Contamination by the irradiated M dwarf can be recognized in the optical spectra (Gianninas et al. 2011; Guo et al. 2015). However, the optical spectrum we obtained from MWDD (Gianninas et al. 2011) does not cover the  $H\alpha$  region and is not contaminated. As a result of stringent error margins imposed in this work ( $T_{\text{eff}} = 63 \pm 3$  kK and  $\log g = 7.5 \pm 0.2$ ), only 5 of 15 previously reported  $T_{\text{eff}}$  and  $\log g$  combinations statistically agree with ours, though deviations in  $T_{\text{eff}}$  do not exceed 8 kK. In contrast, a comparison of abundances with former studies (Vennes et al. 1992, 2000; Barstow et al. 2003b, 2014) reveals a consistent outcome, except for the mismatch in Ni and C abundances derived by Barstow et al. (2003b, 2014), respectively. CNO being on the lower end, we measured below solar abundances for all elements. Among these, only the Fe abundance is in agreement with the diffusion theory (Chayer et al. 1995b). Since this object has comparable metal abundances to DA WDs with similar parameters, accretion of wind material from the M dwarf is unlikely.

**WD 0311+480** FUSE spectra of this DA WD are heavily contaminated by interstellar absorption, which substantially hinders the measurement of stellar parameters. Only the  $C_{\text{III}}$  and  $C_{\text{IV}}$  ionization balance provided a constraint for the temperature. Therefore, setting a large error range was needed ( $T_{\text{eff}} = 70 \pm 10$  kK). Also, successfully fitting all the Balmer lines was not possible. We managed to replicate line cores other than  $H\beta$ , which is too deep in the observation. However, line wings of  $H\delta$  and  $H\epsilon$  are slightly broader in our model. The higher order members of the Balmer-line series, as well as the Lyman lines in the FUSE spectrum, indicate a higher gravity; thus, we opted for  $\log g = 7.3 \pm 0.4$ . To the best of our knowledge, spectroscopic parameters of this object were previously derived only by Gianninas et al. (2010,  $T_{\text{eff}} = 97.8$  kK and  $\log g = 6.96$ ). Although they utilized three different grids containing H/He, solar-CNO, and  $10 \times$  solar-CNO models, the inclusion of light metals, even in large quantities, did not prevent the Balmer-line problem. Their best-fit parameters were derived from the models that include solar-CNO. However, analyzing FUSE spectra uncovered a sub-solar light metal content, including CNO. In contrast, a slight Fe and Ni enhancement was detected. Except for C, Si, and Fe, we present upper-limit abundances. Only C, N, and Fe abundances yield results similar to predictions of the diffusion theory (Chayer et al. 1995b).

**WD 0343-007** We derived  $T_{\text{eff}} = 63 \pm 4$  kK and  $\log g = 7.7 \pm 0.2$ , which are statistically in perfect agreement with previous results from optical spectroscopy (Babel 1995; Finley et al. 1997; Lajoie & Bergeron 2007; Koester et al. 2009; Limoges & Bergeron 2010; Gianninas et al. 2011). All of the element abundances were derived as sub-solar, while the depletion is less than 0.3 dex sub-solar for P, Fe and Ni. Excluding Si and S, element abundances are given as upper limits. Only the Fe abundance agrees with the theoretical calculations of Chayer et al. (1995b).

**WD 0455-282** Previously, EUV, FUV, and optical analyses of this DA WD have been made multiple times. However, we found that only values derived by Limoges & Bergeron (2010) reside within our  $T_{\text{eff}} = 66 \pm 3$  kK and  $\log g = 7.5 \pm 0.2$  boundaries in the Kiel diagram. Nonetheless, the temperature differences to our lower and upper limits are smaller than 10 kK and 3 kK, respectively, while early studies except for a few reported

a tendency of  $\log g \geq 7.80$ . As previously stated, the Balmer-line problem was not detected in our optical fits. We measured sub-solar element abundances, with C, N, O, and Fe, Ni being extremely and slightly depleted, respectively. Only the Fe abundance is consistent with diffusion theory. Our element abundances generally agree with Vennes et al. (1996) and Preval et al. (2019) except for the differences in P and C, respectively. Also, among C, N, O, Si, Fe, Ni, O and Si are the only elements that show a large discrepancy compared to Barstow et al. (2003b). In contrast, C and S measurements of Barstow et al. (2014) significantly differ from ours, whereas Si and  $P^8$  remain in our error range.

**WD 0615+655** is the hottest DA WD in our sample ( $T_{\text{eff}} = 83 \pm 10$  kK and  $\log g = 7.6 \pm 0.4$ ). While  $T_{\text{eff}}$  and  $\log g$  derived by Homeier et al. (1998) and Lajoie & Bergeron (2007) lie out of our range, our results are in agreement with Gianninas et al. (2010). However, we were unable to fit the line core of  $H\beta$ , whereas other Balmer lines are reproduced better. Element abundances were measured by utilizing HST spectra, except for P, which shows no lines in the HST wavelength range. A slightly sub-solar upper limit was estimated for P from FUSE spectra. Fe and Ni are the only species derived above the solar value. The remaining elements were found to be sub-solar. C, P, S, and Fe abundances match with theoretical predictions (Chayer et al. 1995b).

**WD 0621-376** Exploiting multiple ionization balances e.g.  $C_{\text{III}}/C_{\text{IV}}$ ,  $O_{\text{IV}}/O_{\text{V}}$ ,  $P_{\text{IV}}/P_{\text{V}}$ ,  $Fe_{\text{V}}/Fe_{\text{VI}}$ , and  $Ni_{\text{V}}/Ni_{\text{VI}}$  enabled us to constrain the temperature tightly ( $T_{\text{eff}} = 65 \pm 3$  kK). Thanks to high S/N FUSE spectra and dearth of ISM contribution, a perfect fit to Lyman lines could be achieved with  $\log g = 7.5$ . On the other hand, except for the higher orders, the same parameters resulted in poor Balmer-line fits, emerging as deeper line cores and narrower wings of  $H\delta - H\alpha$ . Decreasing  $\log g$  to 7.10 solved the issue for deep lines but diminished the quality of higher-order line fits; therefore, imposing a large error limit was inevitable  $\log g = 7.5 \pm 0.4$ . In comparison, other studies in various bands report a lower  $\log g$ , excluding Barstow et al. (2003b) and Preval et al. (2019) which report similar results. On the other hand, previous abundance measurements reside either within or slightly out of our error limits (Holberg et al. 1993; Barstow et al. 2003b, 2014; Preval et al. 2019). However, C and N abundances derived by Barstow et al. (2014) and Holberg et al. (1993) significantly differ from our parameters, respectively. Our study indicates sub-solar light metal and roughly solar Fe and Ni content. C, O, and Fe abundances are comparable to the diffusion theory.

**WD 0939+262** is the only DA WD in our sample without a FUSE spectrum. Consequently, we could not derive the P abundance for this object since relevant P lines are only found in the FUSE wavelength range. We derived  $T_{\text{eff}} = 66 \pm 3$  kK and  $\log g = 7.7 \pm 0.2$ . With Si indicating an upper limit, light metals are heavily depleted compared to the Sun, while Fe and Ni were measured as slightly sub-solar. Only the Fe abundance coincides with the theoretical predictions. All abundances derived by Barstow et al. (2003b) are within our error range, but Fe and Ni. Only  $T_{\text{eff}}$  and  $\log g$  determined by Liebert et al. (2005) and Lajoie & Bergeron (2007) are statistically in agreement within set limits in the Kiel diagram.

<sup>8</sup> Barstow et al. (2014) provide P abundances determined by fitting  $P_{\text{IV}}$  and  $P_{\text{V}}$  lines. Their measurements from  $P_{\text{V}}$  lines are very similar to ours, though abundances determined from  $P_{\text{IV}}$  lie  $\sim 0.3$  dex below our error range.

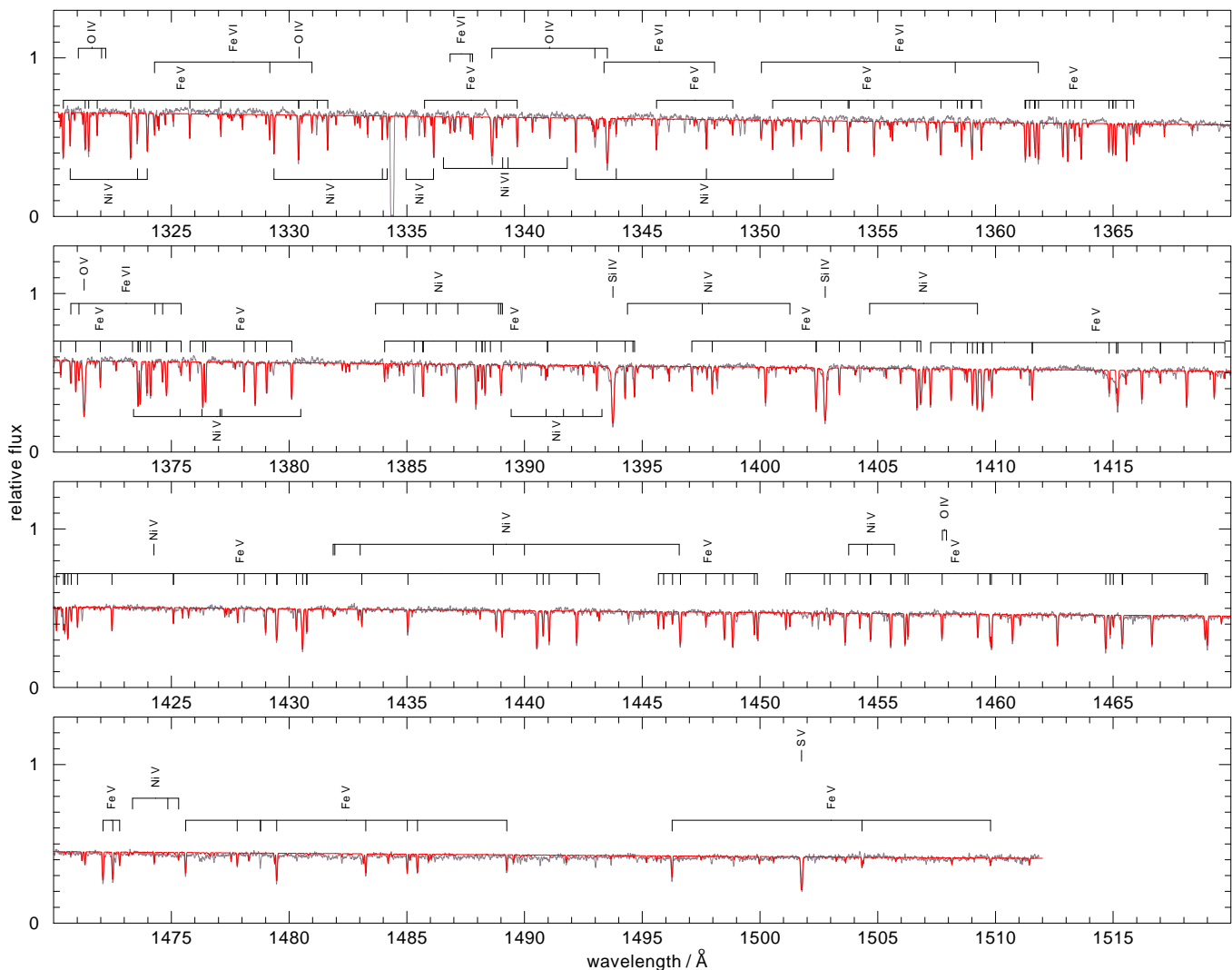


Fig. A.2: HST spectrum of the DA WD 2211–495 (red: model with  $T_{\text{eff}} = 68$  kK,  $\log g = 7.4$ ).

**WD 1056+516** FUSE spectra of this DA WD indicate extremely low metal content. Due to poor data quality, detecting any photospheric line was not possible. Therefore, we increased the element abundances to upper limits where the model lines disappear in the noise of the observation. Adamczak et al. (2012) reports similar upper limits from the analysis of the FUSE spectra. However, they opt for a lower temperature ( $T_{\text{eff}} = 56 \pm 2$  kK,  $\log g = 7.90 \pm 0.3$ ) due to the EUV flux of the *Chandra* spectrum, which is slightly below our error limit. We estimate  $T_{\text{eff}} = 63 \pm 5$  kK and  $\log g = 7.9 \pm 0.2$ . Parameters derived by Vennes et al. (1997), Lajoie & Bergeron (2007), and Bédard et al. (2020) through Balmer-line fitting statistically agree with ours.

**WD 1342+443** We derived  $T_{\text{eff}} = 62 \pm 5$  kK and  $\log g = 7.7 \pm 0.3$ , which statistically only agree with parameters measured by Barstow et al. (2014). Both the MWDD and SDSS spectra of this object show unusually weak  $H\beta$ , while we could reproduce the remaining Balmer lines accurately. This might explain the large disparity between FUV and optical analyses, which tend to find higher  $T_{\text{eff}}$  and  $\log g$ . We measured sub-solar abundances for all elements, among which C, N, O, Fe, and Ni were given as upper limits. Our results partially agree with abundances derived by Barstow et al. (2003b, 2014), who derived C, O, Si, Fe, and Ni;

and C, Si, P, and S, respectively. From their first study, O and Si, and their second study, Si, P, and S abundances are comparable to ours.

**WD 1738+669** is one of the hottest DA WDs in our sample ( $T_{\text{eff}} = 78 \pm 6$  kK and  $\log g = 7.6 \pm 0.4$ ). Temperature and surface gravity derived by Lajoie & Bergeron (2007) and Gianninas et al. (2010) through Balmer-line fitting and by Barstow et al. (2003a) through Lyman-line fitting statistically agree with our results. Light-metal abundances were measured as sub-solar, whereas Fe and Ni show solar abundance. Only the Fe abundance is comparable to theoretical predictions. We find an agreement with light metal abundances determined by Barstow et al. (2003b), whereas their Fe and Ni abundances are significantly lower than ours.

**WD 1827+778** This object shows a high metal content compared to the rest of the DAs in our sample. All light metals were measured close to solar value except O and Si, whereas Fe and Ni are slightly over solar. However, these results might be deemed questionable due to the poor quality of the FUSE spectra, which also complicated the ionization balance assessment. Therefore, a wider error margin had to be imposed on temperature ( $T_{\text{eff}} = 78 \pm 10$  kK). Uncertainty on the surface gravity is

also large due to the line core of  $H\beta$  being weaker in our model ( $\log g = 7.4 \pm 0.4$ ).

**WD 2046+396** We estimate  $T_{\text{eff}} = 64 \pm 5$  kK and  $\log g = 7.8 \pm 0.3$  for this DA WD. The uncertainty in  $\log g$  arises from poor fits to  $H\alpha$  and  $H\beta$  that indicate a lower  $\log g$ . However, this contradicts what was inferred from Lyman and higher-order Balmer lines. In general, these results are in agreement with previous works (Finley et al. 1997; Lajoie & Bergeron 2007; Gianninas et al. 2011; Lépine et al. 2011). Additionally, all element abundances were measured as sub-solar, and only the Fe abundance was comparable to diffusion theory.

**WD 2146–433** Due to good quality FUSE spectra, we were able to use multiple ionization balances. Hence, we could impose a tight constraint on the temperature ( $T_{\text{eff}} = 66 \pm 4$  kK). Moreover, metal abundances for this object were measured as sub-solar, excluding P, Fe, and Ni, which are roughly solar. These abundances are in agreement with those derived by Barstow et al. (2014) except for Si. In addition, Fe and P abundances match with theoretical predictions by Chayer et al. (1995b) and Vennes et al. (1996), respectively. Generally, both Lyman and Balmer lines indicate a similar gravity ( $\log g = 7.5 \pm 0.3$ ), though a slight mismatch between the observed and model spectrum of  $H\beta$  enforces a rather high error range for  $\log g$ .

**WD 2211–495** We utilized FUSE, HST, UVES, and MWDD spectra to determine the parameters of this object ( $T_{\text{eff}} = 68 \pm 4$  kK and  $\log g = 7.4 \pm 0.3$ ). Thanks to the high S/N of the UV spectra,  $T_{\text{eff}}$  and metal abundances could be measured precisely. However, like WD 0621–376, the surface gravity inferred from Lyman and Balmer lines indicates different values. While  $\log g = 7.10$  reproduces  $H\alpha$  and  $H\beta$  in both MWDD and UVES spectra,  $\log g = 7.40$  perfectly fits Lyman lines and up to  $H\gamma$ . Most of the previous analyses report  $T_{\text{eff}}$  and  $\log g$  within our error limits. Except for P, Fe, and Ni, sub-solar metal abundances were measured. Our abundances are in agreement with those derived by Holberg et al. (1993), Barstow et al. (2003b), and Preval et al. (2019), where only mismatch occurs in N abundance for the former two analyses. On the other hand, excluding S, Barstow et al. (2014) reports much lower light metal content than ours. Our C and Fe abundances are comparable to theoretical predictions.

**WD 2218+706** is the only DA WD in our sample that displays a weak  $\text{He II } \lambda 1640 \text{ \AA}$  feature. We derived  $N(\text{He})/N(\text{H}) = 1.3 \times 10^{-4}$ , which is the highest among DAs in our sample and clearly lower than the estimated He abundance limit (Fig. A.3). We estimate  $T_{\text{eff}} = 78 \pm 5$  kK and  $\log g = 7.4 \pm 0.3$ , which statistically agrees only with values derived by Gianninas et al. (2010). Moreover, we derived light metal abundances as sub-solar, while Fe and Ni are slightly over solar. Interestingly, WD 2218+706 is the only DA WD in our sample that shows element abundances close to the theoretical predictions, where C, N, O, and Fe abundances agree very well, and S and P slightly lie outside of our error limits.

**WD 2350–706** HD 223816 is a wide binary system consisting of an F5IV star and a DA WD (Barstow et al. 1994), which has been resolved in HST imaging (Barstow et al. 2001b). We determined  $T_{\text{eff}} = 75 \pm 5$  kK and  $\log g = 7.9 \pm 0.3$  for the WD of the system. Since we did not have optical spectra, the  $\log g$  error could only be assessed by Lyman lines. Our  $T_{\text{eff}}$  and  $\log g$  values agree with those determined by Barstow et al. (2014) and Joyce et al. (2018). On the other hand, only Si and S abundances derived by Barstow et al. (2014) reside in our error range. We find C, P, and Fe abundances similar to theoretical predictions.

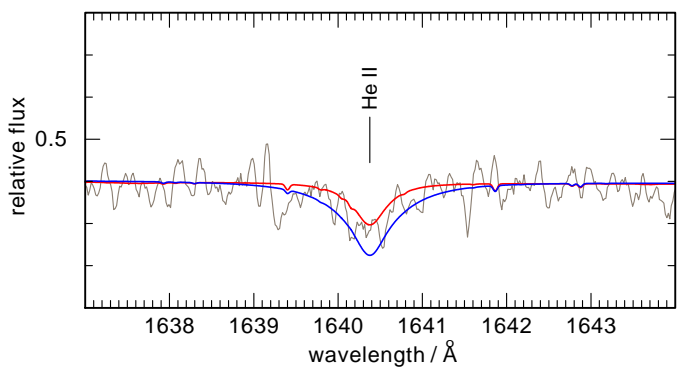


Fig. A.3: Section of the STIS spectrum (gray) of the DA WD 2218+706 compared to models ( $T_{\text{eff}} = 78$  kK,  $\log g = 7.4$ ) with measured He abundance (red;  $N(\text{He})/N(\text{H}) = 1.3 \times 10^{-4}$ ) and theoretical He limit (blue;  $N(\text{He})/N(\text{H}) = 10^{-3}$ ).

**WD 2353+026** This DA WD has poor quality FUSE spectra. Considering the low metal content, distinguishing spectral lines from noise was not possible. Therefore, all abundances are given as upper limits. We derived  $T_{\text{eff}} = 61 \pm 5$  kK and  $\log g = 7.5 \pm 0.3$  which agrees with the previous studies.

## Appendix B: Tables

Table B.1: Our WD sample and observations used in the spectral analysis.

WD Name <sup>(a)</sup>	Other Name	Program ID (FUSE)	Proposal ID (HST)	Optical <sup>(b)</sup>
		DAO		
	Longmore 1	P133	–	UVES
0439+466	LS V +46 21	M107	8638	G10
0500–156	Abell 7	B052	–	G10
0615+556	PuWe 1	B052	–	G10
0823+316	Ton 320	B053	–	G10
0834+500	PG 0834+501	B053	–	G10
0851+090	Abell 31	B052	–	UVES
1111+552	NGC 3587	B052	–	-
1214+267	LB 2	B053	–	G10
1253+378	HZ 34	B053	–	G10
1957+225	NGC 6853	M107	8638	G10
2226–210	NGC 7293	C177	8638	G10
2342+806	GD 561	B052	8329	G10
		DA		
0027–636	RE J0029–632	Z903	–	G11
0229–481	LB 1628	M105	–	G11
0232+035	Feige 24	P104	7755	G11
0311+480	KPD 0311+4801	Z904	–	G10
0343–007	KUV03439–0048	E568	–	G11
0455–282	RE J0457–280	P104	14791	G10
0615+655	HS 0615+6535	E568	8636	G10
0621–376	RE J0623–374	P104	14791	G10, UVES
0939+262	Ton 21	–	8179	G11
1056+516	LB 1919	D003	–	G11, SDSS
1342+443	PG 1342+444	A034	–	G11, SDSS
1738+669	RE J1738+665	M105	8179	G10
1827+778	HS 1827+7753	E568	–	G11, SDSS
2046+396	KPD 2046+3940	E568	–	G11
2146–433	MCT2146–4320	Z903	–	G10
2211–495	RE J2214–491	M103	14791	G10, UVES
2218+706	DeHt 5	A034	8179	G10
2350–706	HD 223816	B120, A054	–	–
2353+026	PG 2353+027	E568	–	G11

**Notes.** <sup>(a)</sup> WD names from [McCook & Sion \(1999\)](#). <sup>(b)</sup> G10 and G11 refer to MWDD spectra used in [Gianninas et al. \(2010, 2011\)](#), respectively.

Table B.2:  $T_{\text{eff}}$ ,  $\log g$ , and abundances (mass fractions) of DAO and DA WDs.

(WD) Name	$T_{\text{eff}}$ [kK]	$\log g$ [cm/s <sup>2</sup> ]	H	He	C	N	O	Si	P	S	Fe	Ni
Longmore 1	118 ± 5	7.0 ± 0.3	6.93 × 10 <sup>-1</sup>	2.45 × 10 <sup>-1</sup>	1.74 × 10 <sup>-2</sup>	8.69 × 10 <sup>-3</sup>	3.29 × 10 <sup>-2</sup>	1.63 × 10 <sup>-4</sup>	5.81 × 10 <sup>-6</sup>	3.08 × 10 <sup>-4</sup>	2.40 × 10 <sup>-3</sup>	6.78 × 10 <sup>-5</sup>
0439+466	97 ± 5	7.0 ± 0.2	9.57 × 10 <sup>-1</sup>	3.16 × 10 <sup>-2</sup>	1.15 × 10 <sup>-3</sup>	8.18 × 10 <sup>-4</sup>	2.69 × 10 <sup>-3</sup>	2.71 × 10 <sup>-4</sup>	3.79 × 10 <sup>-6</sup>	7.54 × 10 <sup>-5</sup>	6.20 × 10 <sup>-3</sup>	2.98 × 10 <sup>-4</sup>
0500–156	104 ± 6	7.2 ± 0.2	8.61 × 10 <sup>-1</sup>	1.25 × 10 <sup>-1</sup>	2.67 × 10 <sup>-3</sup>	2.95 × 10 <sup>-4</sup>	8.37 × 10 <sup>-3</sup>	1.65 × 10 <sup>-4</sup>	1.82 × 10 <sup>-6</sup>	3.90 × 10 <sup>-5</sup>	2.61 × 10 <sup>-3</sup>	1.48 × 10 <sup>-4</sup>
0615+556	101 ± 5	7.2 ± 0.2	9.35 × 10 <sup>-1</sup>	5.56 × 10 <sup>-2</sup>	2.68 × 10 <sup>-3</sup>	2.95 × 10 <sup>-4</sup>	3.39 × 10 <sup>-3</sup>	1.42 × 10 <sup>-4</sup>	1.39 × 10 <sup>-5</sup>	1.19 × 10 <sup>-4</sup>	2.52 × 10 <sup>-3</sup>	2.49 × 10 <sup>-4</sup>
0823+316	98 ± 5	7.1 ± 0.2	9.75 × 10 <sup>-1</sup>	1.52 × 10 <sup>-2</sup>	2.77 × 10 <sup>-3</sup>	1.09 × 10 <sup>-3</sup>	2.55 × 10 <sup>-3</sup>	2.63 × 10 <sup>-4</sup>	5.81 × 10 <sup>-6</sup>	4.88 × 10 <sup>-5</sup>	2.70 × 10 <sup>-3</sup>	1.28 × 10 <sup>-4</sup>
0834+500	90 ± 3	7.0 ± 0.2	9.73 × 10 <sup>-1</sup>	1.82 × 10 <sup>-2</sup>	4.72 × 10 <sup>-4</sup>	1.84 × 10 <sup>-3</sup>	1.75 × 10 <sup>-3</sup>	1.22 × 10 <sup>-4</sup>	6.30 × 10 <sup>-6</sup>	7.44 × 10 <sup>-5</sup>	4.30 × 10 <sup>-3</sup>	3.47 × 10 <sup>-4</sup>
0851+090	106 ± 5	7.2 ± 0.2	8.60 × 10 <sup>-1</sup>	1.25 × 10 <sup>-1</sup>	2.87 × 10 <sup>-3</sup>	4.95 × 10 <sup>-4</sup>	8.37 × 10 <sup>-3</sup>	1.65 × 10 <sup>-4</sup>	5.82 × 10 <sup>-6</sup>	5.90 × 10 <sup>-5</sup>	2.51 × 10 <sup>-3</sup>	2.08 × 10 <sup>-4</sup>
1111+552	110 ± 5	7.1 ± 0.3	7.82 × 10 <sup>-1</sup>	2.07 × 10 <sup>-1</sup>	3.66 × 10 <sup>-3</sup>	4.25 × 10 <sup>-4</sup>	5.24 × 10 <sup>-3</sup>	1.22 × 10 <sup>-4</sup>	3.81 × 10 <sup>-6</sup>	4.87 × 10 <sup>-5</sup>	1.30 × 10 <sup>-3</sup>	1.30 × 10 <sup>-4</sup>
1214+267	91 ± 3	7.1 ± 0.3	9.69 × 10 <sup>-1</sup>	2.42 × 10 <sup>-2</sup>	6.73 × 10 <sup>-4</sup>	6.94 × 10 <sup>-4</sup>	1.75 × 10 <sup>-3</sup>	2.42 × 10 <sup>-4</sup>	6.20 × 10 <sup>-6</sup>	2.87 × 10 <sup>-5</sup>	1.93 × 10 <sup>-3</sup>	1.18 × 10 <sup>-4</sup>
1253+378	93 ± 4	7.0 ± 0.2	9.50 × 10 <sup>-1</sup>	4.07 × 10 <sup>-2</sup>	1.10 × 10 <sup>-3</sup>	7.22 × 10 <sup>-5</sup>	3.50 × 10 <sup>-3</sup>	5.00 × 10 <sup>-5</sup>	3.78 × 10 <sup>-6</sup>	3.72 × 10 <sup>-5</sup>	3.39 × 10 <sup>-3</sup>	1.18 × 10 <sup>-4</sup>
1957+225	134 ± 10	6.9 ± 0.4	7.39 × 10 <sup>-1</sup>	2.50 × 10 <sup>-1</sup>	2.36 × 10 <sup>-3</sup>	6.98 × 10 <sup>-4</sup>	5.77 × 10 <sup>-3</sup>	2.05 × 10 <sup>-4</sup>	5.55 × 10 <sup>-6</sup>	1.61 × 10 <sup>-4</sup>	1.21 × 10 <sup>-3</sup>	6.80 × 10 <sup>-5</sup>
2226–210	120 ± 5	7.2 ± 0.3	8.80 × 10 <sup>-1</sup>	1.05 × 10 <sup>-1</sup>	2.36 × 10 <sup>-3</sup>	6.94 × 10 <sup>-4</sup>	1.93 × 10 <sup>-3</sup>	2.03 × 10 <sup>-4</sup>	5.81 × 10 <sup>-6</sup>	1.08 × 10 <sup>-4</sup>	9.40 × 10 <sup>-3</sup>	3.08 × 10 <sup>-4</sup>
2342+806	83 ± 5	7.2 ± 0.2	9.74 × 10 <sup>-1</sup>	1.63 × 10 <sup>-2</sup>	1.57 × 10 <sup>-3</sup>	1.94 × 10 <sup>-4</sup>	1.96 × 10 <sup>-3</sup>	2.43 × 10 <sup>-4</sup>	5.81 × 10 <sup>-6</sup>	1.09 × 10 <sup>-4</sup>	5.22 × 10 <sup>-3</sup>	3.88 × 10 <sup>-4</sup>
0027–636	59 ± 5	8.0 ± 0.2	9.99 × 10 <sup>-1</sup>	3.98 × 10 <sup>-5</sup>	1.05 × 10 <sup>-6</sup>	5.04 × 10 <sup>-7</sup>	9.04 × 10 <sup>-6</sup>	3.32 × 10 <sup>-7</sup>	3.20 × 10 <sup>-8</sup>	4.30 × 10 <sup>-7</sup>	3.98 × 10 <sup>-4</sup>	3.49 × 10 <sup>-5</sup>
0229–481	62 ± 5	7.8 ± 0.2	9.99 × 10 <sup>-1</sup>	1.98 × 10 <sup>-5</sup>	1.14 × 10 <sup>-6</sup>	1.08 × 10 <sup>-7</sup>	8.80 × 10 <sup>-7</sup>	9.22 × 10 <sup>-6</sup>	2.30 × 10 <sup>-6</sup>	4.98 × 10 <sup>-6</sup>	4.51 × 10 <sup>-4</sup>	3.49 × 10 <sup>-5</sup>
0232+035	63 ± 3	7.5 ± 0.2	9.99 × 10 <sup>-1</sup>	5.98 × 10 <sup>-5</sup>	1.45 × 10 <sup>-6</sup>	1.61 × 10 <sup>-6</sup>	1.04 × 10 <sup>-5</sup>	2.16 × 10 <sup>-5</sup>	3.14 × 10 <sup>-6</sup>	8.80 × 10 <sup>-6</sup>	6.20 × 10 <sup>-4</sup>	4.81 × 10 <sup>-5</sup>
0311+480	70 ± 10	7.3 ± 0.4	9.98 × 10 <sup>-1</sup>	1.98 × 10 <sup>-5</sup>	5.55 × 10 <sup>-5</sup>	2.14 × 10 <sup>-4</sup>	1.11 × 10 <sup>-5</sup>	5.22 × 10 <sup>-5</sup>	1.50 × 10 <sup>-6</sup>	1.58 × 10 <sup>-5</sup>	1.80 × 10 <sup>-3</sup>	1.38 × 10 <sup>-4</sup>
0343–007	63 ± 4	7.7 ± 0.2	9.99 × 10 <sup>-1</sup>	1.98 × 10 <sup>-5</sup>	1.85 × 10 <sup>-6</sup>	2.08 × 10 <sup>-6</sup>	8.10 × 10 <sup>-6</sup>	1.22 × 10 <sup>-5</sup>	3.50 × 10 <sup>-6</sup>	5.78 × 10 <sup>-6</sup>	6.91 × 10 <sup>-4</sup>	4.48 × 10 <sup>-5</sup>
0455–282	66 ± 3	7.5 ± 0.2	9.99 × 10 <sup>-1</sup>	3.98 × 10 <sup>-5</sup>	1.45 × 10 <sup>-6</sup>	1.61 × 10 <sup>-6</sup>	5.69 × 10 <sup>-6</sup>	2.16 × 10 <sup>-5</sup>	3.14 × 10 <sup>-6</sup>	8.80 × 10 <sup>-6</sup>	5.20 × 10 <sup>-4</sup>	3.20 × 10 <sup>-5</sup>
0615+655	83 ± 10	7.6 ± 0.4	9.97 × 10 <sup>-1</sup>	3.98 × 10 <sup>-5</sup>	1.45 × 10 <sup>-5</sup>	7.84 × 10 <sup>-6</sup>	3.61 × 10 <sup>-5</sup>	6.42 × 10 <sup>-5</sup>	5.20 × 10 <sup>-6</sup>	7.98 × 10 <sup>-5</sup>	2.51 × 10 <sup>-3</sup>	1.35 × 10 <sup>-4</sup>
0621–376	65 ± 3	7.5 ± 0.4	9.98 × 10 <sup>-1</sup>	1.98 × 10 <sup>-5</sup>	1.06 × 10 <sup>-5</sup>	1.08 × 10 <sup>-5</sup>	3.22 × 10 <sup>-5</sup>	5.22 × 10 <sup>-5</sup>	4.20 × 10 <sup>-6</sup>	1.30 × 10 <sup>-5</sup>	1.72 × 10 <sup>-3</sup>	1.36 × 10 <sup>-4</sup>
0939+262	66 ± 3	7.7 ± 0.2	9.99 × 10 <sup>-1</sup>	3.98 × 10 <sup>-5</sup>	1.45 × 10 <sup>-6</sup>	1.61 × 10 <sup>-6</sup>	3.69 × 10 <sup>-6</sup>	2.16 × 10 <sup>-5</sup>	4.20 × 10 <sup>-6</sup>	8.80 × 10 <sup>-6</sup>	5.20 × 10 <sup>-4</sup>	3.40 × 10 <sup>-5</sup>
1056+516	63 ± 5	7.9 ± 0.2	9.99 × 10 <sup>-1</sup>	1.98 × 10 <sup>-5</sup>	1.15 × 10 <sup>-6</sup>	5.84 × 10 <sup>-7</sup>	3.10 × 10 <sup>-6</sup>	1.11 × 10 <sup>-7</sup>	8.49 × 10 <sup>-9</sup>	7.77 × 10 <sup>-7</sup>	2.54 × 10 <sup>-4</sup>	2.89 × 10 <sup>-5</sup>
1342+443	62 ± 5	7.7 ± 0.3	9.99 × 10 <sup>-1</sup>	1.98 × 10 <sup>-5</sup>	6.48 × 10 <sup>-6</sup>	2.08 × 10 <sup>-6</sup>	5.10 × 10 <sup>-5</sup>	6.22 × 10 <sup>-6</sup>	3.50 × 10 <sup>-6</sup>	1.28 × 10 <sup>-5</sup>	5.04 × 10 <sup>-4</sup>	3.88 × 10 <sup>-5</sup>
1738+669	78 ± 6	7.6 ± 0.4	9.99 × 10 <sup>-1</sup>	9.18 × 10 <sup>-5</sup>	2.08 × 10 <sup>-6</sup>	2.04 × 10 <sup>-6</sup>	4.25 × 10 <sup>-6</sup>	1.84 × 10 <sup>-5</sup>	1.40 × 10 <sup>-6</sup>	1.78 × 10 <sup>-5</sup>	1.10 × 10 <sup>-3</sup>	6.09 × 10 <sup>-5</sup>
1827+778	78 ± 10	7.4 ± 0.4	9.98 × 10 <sup>-1</sup>	1.98 × 10 <sup>-5</sup>	1.59 × 10 <sup>-4</sup>	1.74 × 10 <sup>-4</sup>	4.04 × 10 <sup>-6</sup>	3.62 × 10 <sup>-5</sup>	6.00 × 10 <sup>-6</sup>	1.16 × 10 <sup>-4</sup>	1.69 × 10 <sup>-3</sup>	1.03 × 10 <sup>-4</sup>
2046+396	64 ± 5	7.8 ± 0.3	9.99 × 10 <sup>-1</sup>	1.98 × 10 <sup>-5</sup>	1.15 × 10 <sup>-6</sup>	4.84 × 10 <sup>-7</sup>	5.23 × 10 <sup>-7</sup>	7.21 × 10 <sup>-6</sup>	2.50 × 10 <sup>-6</sup>	5.17 × 10 <sup>-6</sup>	5.04 × 10 <sup>-4</sup>	4.64 × 10 <sup>-5</sup>
2146–433	66 ± 4	7.5 ± 0.3	9.99 × 10 <sup>-1</sup>	1.98 × 10 <sup>-5</sup>	6.15 × 10 <sup>-6</sup>	4.08 × 10 <sup>-6</sup>	4.23 × 10 <sup>-7</sup>	4.72 × 10 <sup>-5</sup>	7.50 × 10 <sup>-6</sup>	5.77 × 10 <sup>-6</sup>	1.23 × 10 <sup>-3</sup>	6.49 × 10 <sup>-5</sup>
2211–495	68 ± 4	7.4 ± 0.3	9.98 × 10 <sup>-1</sup>	1.98 × 10 <sup>-5</sup>	1.35 × 10 <sup>-5</sup>	1.08 × 10 <sup>-5</sup>	2.63 × 10 <sup>-5</sup>	5.62 × 10 <sup>-5</sup>	7.49 × 10 <sup>-6</sup>	3.08 × 10 <sup>-5</sup>	1.61 × 10 <sup>-3</sup>	1.27 × 10 <sup>-4</sup>
2218+706	78 ± 5	7.4 ± 0.3	9.96 × 10 <sup>-1</sup>	5.10 × 10 <sup>-4</sup>	9.45 × 10 <sup>-5</sup>	1.12 × 10 <sup>-4</sup>	1.26 × 10 <sup>-4</sup>	6.42 × 10 <sup>-5</sup>	5.20 × 10 <sup>-6</sup>	4.58 × 10 <sup>-5</sup>	2.81 × 10 <sup>-3</sup>	2.15 × 10 <sup>-4</sup>
2350–706	75 ± 5	7.9 ± 0.3	9.99 × 10 <sup>-1</sup>	1.98 × 10 <sup>-5</sup>	8.15 × 10 <sup>-6</sup>	1.08 × 10 <sup>-6</sup>	3.32 × 10 <sup>-7</sup>	5.62 × 10 <sup>-5</sup>	9.95 × 10 <sup>-6</sup>	1.88 × 10 <sup>-5</sup>	6.04 × 10 <sup>-4</sup>	4.58 × 10 <sup>-5</sup>
2353+026	61 ± 5	7.5 ± 0.3	9.99 × 10 <sup>-1</sup>	1.98 × 10 <sup>-5</sup>	7.59 × 10 <sup>-6</sup>	1.08 × 10 <sup>-6</sup>	7.38 × 10 <sup>-7</sup>	1.97 × 10 <sup>-7</sup>	2.11 × 10 <sup>-8</sup>	3.08 × 10 <sup>-6</sup>	4.99 × 10 <sup>-4</sup>	2.48 × 10 <sup>-5</sup>

**Notes.** Upper limits are marked with triangles. Error limits for abundances do not exceed ± 0.5 dex.

Table B.3: Previous analyses whose results are compared to the DAO WDs in our sample.

Name	Optical	UV	Optical + UV	Abundances
		DAO		
Longmore 1	(1)	(2), (3)	—	(2), (3)
WD 0439+466	(4), (5), (6)	(7)	(8)	(7), (8)
WD 0500–156	(5), (6), (9), (10), (11), (12)	(3), (12)	—	(3), (13)
WD 0615+556	(5), (6), (11), (12)	(3), (12)	—	(3), (13)
WD 0823+316	(4), (6), (12), (14), (15), (16)	(12)	—	(13)
WD 0834+500	(4), (6), (12)	(12)	—	(13)
WD 0851+090	(5), (12)	(3), (12)	—	(3), (13)
WD 1111+552	(5), (11)	(3)	—	(3)
WD 1214+267	(4), (6), (12), (17)	(12)	—	(13)
WD 1253+378	(4), (5), (6), (10), (12), (18)	(12)	—	(13)
WD 1957+225	(5), (6)	(7)	(3)	(3), (7)
WD 2226–210	(1), (5), (6), (11), (19)	(7)	(3)	(3), (7)
WD 2342+806	(4), (5), (6), (12)	(3), (12)	—	(3), (13)

**References.** <sup>(1)</sup>Mendez et al. (1985), <sup>(2)</sup>Herald & Bianchi (2004), <sup>(3)</sup>Ziegler (2012), <sup>(4)</sup>Bergeron et al. (1994), <sup>(5)</sup>Napiwotzki (1999), <sup>(6)</sup>Gianninas et al. (2010), <sup>(7)</sup>Traulsen et al. (2005), <sup>(8)</sup>Rauch et al. (2007), <sup>(9)</sup>Mendez et al. (1981), <sup>(10)</sup>Wesemael et al. (1985), <sup>(11)</sup>McCarthy et al. (1997), <sup>(12)</sup>Good et al. (2004), <sup>(13)</sup>Good et al. (2005b), <sup>(14)</sup>Tremblay et al. (2011), <sup>(15)</sup>Kepler et al. (2019), <sup>(16)</sup>Bédard et al. (2020), <sup>(17)</sup>Guo et al. (2015), <sup>(18)</sup>Lei et al. (2023), <sup>(19)</sup>Mendez et al. (1988).

**Notes.** The second and third columns list studies that only utilized optical and UV data, respectively, or the analyses derived separate parameters for both wavebands, whereas the fourth column displays the ones that reached a common  $T_{\text{eff}}$  and  $\log g$  from both wavelength ranges. The fifth column lists works that performed abundance analyses.

Table B.4: Like Table B.3, but for DAs and including EUV analyses as well.

Name	Optical	UV	EUV	Optical + UV	Abundances
WD 0027–636	(1), (2), (3), (4), (5), (6), (7), (8)	(5), (9)	(10)	—	—
WD 0229–481	(1), (2), (6), (7), (11), (12), (13)	(9), (13)	—	—	(9)
WD 0232+035	(1), (2), (3), (7), (13), (14), (15)	(5), (9), (13), (16), (17), (18), (19)	(10), (20)	—	(9), (14), (17), (18)
WD 0311+480	(22)	—	—	—	—
WD 0343–007	(1), (6), (7), (11), (13), (23)	(13)	—	—	—
WD 0455–282	(1), (2), (3), (5), (6), (8), (12), (13), (14), (22), (24), (25)	(5), (9), (21), (24), (26), (27)	(10)	(24)	(9), (14), (26), (27)
WD 0615+655	(13), (22), (28),	(13)	—	—	—
WD 0621–376	(1), (2), (3), (5), (6), (13), (14), (22), (25)	(5), (9), (13), (21), (27)	(10)	(29)	(9), (14), (27), (29)
WD 0939+262	(1), (7), (13), (14), (30), (31)	(13)	—	—	(14)
WD 1056+516	(3), (7), (13), (32), (33), (34), (35)	(13), (36)	(10) (36)	—	(36)
WD 1342+443	(7), (14), (30), (31), (33), (34), (35)	(9), (14)	—	(37)	(9), (14), (37)
WD 1738+669	(1), (2), (13), (14), (22)	(13), (21)	—	—	(14)
WD 1827+778	(7), (28), (33), (34), (35)	—	—	—	—
WD 2046+396	(1), (7), (13), (38)	(13)	—	—	—
WD 2146–433	(1), (4), (6), (8), (13), (22)	(9), (13)	—	—	(9)
WD 2211–495	(1), (2), (3), (5), (6), (12), (14), (22), (25)	(5), (9), (21), (27)	(10)	(29)	(9), (14), (27), (29)
WD 2218+706	(14), (22), (39), (40)	(40)	—	(41)	(14), (42)
WD 2350–706	—	(9), (14)	—	—	(9)
WD 2353+026	(1), (4), (6), (7), (13), (28), (31)	(13)	—	—	—

**References.** <sup>(1)</sup>Finley et al. (1997), <sup>(2)</sup>Marsh et al. (1997), <sup>(3)</sup>Vennes et al. (1997), <sup>(4)</sup>Koester et al. (2005), <sup>(5)</sup>Vennes et al. (2005), <sup>(6)</sup>Koester et al. (2009), <sup>(7)</sup>Gianninas et al. (2011), <sup>(8)</sup>Bergeron et al. (2021), <sup>(9)</sup>Barstow et al. (2014), <sup>(10)</sup>Schuh et al. (2002), <sup>(11)</sup>Bragaglia et al. (1995), <sup>(12)</sup>Koester et al. (2001), <sup>(13)</sup>Lajoie & Bergeron (2007), <sup>(14)</sup>Barstow et al. (2003b), <sup>(15)</sup>Bédard et al. (2017), <sup>(16)</sup>Holberg et al. (1986), <sup>(17)</sup>Vennes et al. (1992), <sup>(18)</sup>Vennes et al. (2000), <sup>(19)</sup>Joyce et al. (2018), <sup>(20)</sup>Vennes et al. (1989), <sup>(21)</sup>Barstow et al. (2003a), <sup>(22)</sup>Gianninas et al. (2010), <sup>(23)</sup>Limoges & Bergeron (2010), <sup>(24)</sup>Barstow et al. (1998), <sup>(25)</sup>Kawka et al. (2007), <sup>(26)</sup>Vennes et al. (1996), <sup>(27)</sup>Preval et al. (2019), <sup>(28)</sup>Homeier et al. (1998), <sup>(29)</sup>Holberg et al. (1993), <sup>(30)</sup>Bergeron et al. (1994), <sup>(31)</sup>Liebert et al. (2005), <sup>(32)</sup>Tremblay et al. (2011), <sup>(33)</sup>Kepler et al. (2019), <sup>(34)</sup>Tremblay et al. (2019), <sup>(35)</sup>Bédard et al. (2020), <sup>(36)</sup>Adamczak et al. (2012), <sup>(37)</sup>Barstow et al. (2002), <sup>(38)</sup>Lépine et al. (2011), <sup>(39)</sup>Napiwotzki (1999), <sup>(40)</sup>Good et al. (2004), <sup>(41)</sup>Barstow et al. (2001a), <sup>(42)</sup>Good et al. (2005b)